

Simulating the transport of relativistic electrons and magnetic fields injected by radio galaxies in the intracluster medium[★]

F. Vazza^{1,2,3} , D. Wittor^{2,1}, G. Brunetti³, and M. Brüggen²

¹ Dipartimento di Fisica e Astronomia, Università di Bologna, Via Gobetti 93/2, 40122 Bologna, Italy
e-mail: franco.vazza@unibo.it

² Hamburger Sternwarte, University of Hamburg, Gojenbergsweg 112, 21029 Hamburg, Germany

³ Istituto di Radioastronomia, INAF, Via Gobetti 101, 40122 Bologna, Italy

Received 8 February 2021 / Accepted 20 May 2021

ABSTRACT

Radio galaxies play an important role in the seeding of cosmic rays and magnetic fields in galaxy clusters. Here, we simulate the evolution of relativistic electrons injected into the intracluster medium by radio galaxies. Using passive tracer particles added to magnetohydrodynamical adaptive-mesh simulations, we calculated the evolution of the spectrum of relativistic electrons, taking into account energy losses and re-acceleration mechanisms associated with the dynamics of the intracluster medium. Re-acceleration can occur at shocks via diffusive shock acceleration, and in turbulent flows via second-order Fermi re-acceleration. This study confirms that relativistic electrons from radio galaxies can efficiently fill the intracluster medium over scales of several hundreds of Myr and that they create a stable reservoir of fossil electrons that remains available for further re-acceleration by shock waves and turbulent gas motions. Our results also show that late evolution of radio lobes and remnant radio galaxies is significantly affected by the dynamics of the surrounding intracluster medium. Here, the diffusive re-acceleration couples the evolution of relativistic particles to the gas perturbations. In the near future, deep radio observations, especially at low frequencies, will be able to probe such mechanisms in galaxy clusters.

Key words. acceleration of particles – magnetohydrodynamics (MHD) – radio continuum: general – methods: numerical – galaxies: clusters: intracluster medium

1. Introduction

Galaxy clusters are the largest reservoir of relativistic plasma in the Universe, in which relativistic particles¹ are subject to acceleration and energy losses and are confined by turbulent magnetic fields (e.g. Berezhinsky et al. 1997; Sarazin 1999; Brunetti & Jones 2014; Bykov et al. 2019). Γ -ray observations (e.g. Ackermann et al. 2014) and radio observations (e.g. van Weeren et al. 2019) have provided important constraints on the complex life cycle of relativistic plasma in the intracluster medium (ICM).

Radio-bright, bipolar outflows from active galactic nuclei (AGNs) are commonly found in clusters of galaxies. Radio galaxies play an important role as they have the potential to release large quantities of relativistic plasma and magnetic fields into the ICM (e.g. Völk & Atoyan 1999). Many recent numerical simulations have investigated the dynamics of relativistic jets as they expand into the ambient medium, and the role of magneto-hydrodynamical (MHD) instabilities in determining jet morphology and stability (e.g. Norman et al. 1982; Bodo et al. 1998; Perucho & Martí 2007; Mignone et al. 2005, 2010; Hardcastle & Krause 2014; Massaglia et al. 2016; Borse et al. 2021).

Cosmological simulations predict that radio-mode feedback is crucial for shaping the thermodynamic properties of the gas in

galaxy groups and clusters at low redshifts (e.g. Puchwein et al. 2008; Booth & Schaye 2009; McCourt et al. 2011; Fabjan et al. 2010; Tremmel et al. 2017). At higher redshifts ($z \geq 2-3$), most of the mass growth of supermassive black holes (SMBH) occurs in the radiatively efficient quasar mode, with an accretion rate higher than a few percent of the Eddington rate (e.g. Sijacki et al. 2007).

Observationally, the duty cycle of radio galaxies in the ICM is still poorly constrained. Observations of nearby massive galaxy clusters described in Birzan et al. (2020) concluded that only about half of such systems show clear evidence of radio-mode AGN feedback. Several deep LOFAR observations have discovered steep-spectrum, filamentary, and distorted radio structures, often connecting old tails of radio galaxies with diffuse radio emission across a wide range of spatial scales (Wilber et al. 2018; Botteon et al. 2020a; Mandal et al. 2020). Very recent deep JVLA observations Gendron-Marsolais et al. (2021) have also unveiled complex substructures in the wake of radio galaxy NGC 1272 in the Perseus clusters. Its morphology and spectrum support the possibility that fossil plasma ejected by AGN jets is being re-accelerated by shear and compressive motions in the ICM and that the fossil plasma fuels the mini halo in the Perseus cluster.

The emission from tailed radio galaxies is sometimes linked to diffuse radio emission from the ICM, both in the form of radio halos (Wilber et al. 2018) or radio relics (e.g. Markevitch et al. 2005; Owen et al. 2014; Bonafede et al. 2014; van Weeren et al. 2017; Stuardi et al. 2019). In most cases, a volume-filling distribution of fossil relativistic electrons is required to explain the

[★] Movies associated to Figs. A.1 and A.2 are available at <https://www.aanda.org>

¹ In this paper, we use the terms relativistic particles and cosmic-ray particles interchangeably.

observed radio power (e.g. Brunetti et al. 2001; Markevitch et al. 2005; Kang et al. 2012; Pinzke et al. 2013; Vazza & Brüggen 2014; Vazza et al. 2015; Brunetti & Jones 2014; Kang 2018; Botteon et al. 2020b). The recent ASKAP EMU observation of the merging A3391–3395 pairs of galaxy clusters also detected a three-times-higher sky density of giant radio galaxies (Brüggen et al. 2021) than previously assumed. This suggests that radio jets can have a more significant role in seeding cosmic rays far from their source.

Radio galaxies can also play a role in the genesis of magnetic fields in galaxy clusters (Kronberg et al. 1999; Furlanetto & Loeb 2001; Xu et al. 2009), as they can seed primordial magnetic fields (e.g. Vachaspati 2021, for a recent review). Outside of the virial regions of clusters, the impact of galaxies on extragalactic magnetic fields is expected to be detectable with the next generation of deep radio surveys, both in total intensity and polarisation (e.g. Vazza et al. 2017a; Locatelli et al. 2018). The dynamical interaction between radio jets and the ICM occurs on a wide range of spatial scales ($1 \text{ kpc} \leq L \leq 100 \text{ kpc}$). A number of simulations have given valuable insights into the interaction between AGNs and the surrounding ICM, mostly based on hydrodynamics and starting from the point where the relativistic plasma has reached approximate pressure equilibrium with the surrounding ICM and starts to be dominated by buoyancy (e.g. Churazov et al. 2001; Brüggen & Kaiser 2002; Mathews & Brighenti 2007; Heinz et al. 2006; McCarthy et al. 2010; Gaspari et al. 2011; Yang et al. 2012, 2019).

On the other hand, a few papers have focused on the direct injection of magnetic fields by AGN, and on their impact on the evolution of the ICM. In particular, Xu et al. (2009; 2011) included magnetised outflows from radio galaxies in cosmological ENZO simulations, and studied the build-up of cluster magnetic fields from the injection of individual AGN jets. Mendygral et al. (2012) simulated the effect of ‘cluster weather’ on radio lobes by injecting magnetised jets into a galaxy cluster extracted from a (smoothed particle hydrodynamics) cosmological simulation and re-simulating a cluster cutout region with a grid-based MHD method. This was done in order to evolve radio jets and their magnetic properties at a high resolution. Using the AREPO code, Bourne & Sijacki (2021) performed high-resolution simulations of jets from AGN, and produced realistic X-ray and radio properties (albeit assuming a distribution of magnetic fields and relativistic electrons in post-processing).

In this new work, we devoted more computational resources to the simulation of the properties of non-thermal components injected by jets, while neglecting the effect of gas cooling. Our main focus is on the evolution of radio jets, as well as their magnetic fields and relativistic electrons. In particular, we modelled the evolution of relativistic electrons subject to ageing and acceleration processes. We relied on passive tracers, which in turn did not allow us to study the interplay of a relativistic plasma with the ICM, as has been done in other works (O’Neill & Jones 2010; Mendygral et al. 2012; Nolting et al. 2019a,b). However, our simulations offer an unprecedented view of the large-scale circulation and advection of fossil electrons on megaparsec scales, in a regime scarcely affected by radiative cooling and other processes neglected in this work. They also allow us to test several re-acceleration processes together with a realistic model of the evolving ICM.

Our paper is structured as follows. In Sect. 2, we present the cosmological simulations and numerical methods employed in this paper, while in Sect. 3 we give our results on the evolution of radio sources (3.1), on the impact of radio galaxies on

the ICM (3.2), and on the energy evolution relativistic electrons (3.3). Limitations of our approach are discussed in Sect. 4, and our conclusions are given in Sect. 5.

2. Simulations

2.1. ENZO cosmological simulations

We used the cosmological ENZO-MHD (Bryan et al. 2014) code to produce realistic simulations of the formation of a galaxy group and of the thermal and non-thermal feedback from radio galaxies within it. We use nested grids to provide a uniform resolution at the highest refinement level. Each simulation covers a root-grid of $(50 \text{ Mpc } h^{-1})^3$ and is sampled with 128^3 cells. Using MUSIC (Hahn & Abel 2011), four additional regions with increasing spatial resolution were nested, up to the innermost $(4 \text{ Mpc } h^{-1})^3$ region, where the cluster form is uniformly covered at a $\Delta x = 24.4 \text{ kpc } h^{-1}$ uniform resolution. During the simulation, two additional levels of mesh refinement were added using a local gas or DM overdensity criterion ($\Delta\rho/\rho \geq 3$), allowing the simulation to reach a maximum resolution of $\approx 8.86 \text{ kpc}$, typically in the cluster core region. As a result of our nested grid approach, the mass resolution for dark matter in our cluster formation region is of $m_{\text{DM}} = 2.82 \times 10^6 M_{\odot}$ per dark matter particle for the highest resolution particles that were used to fill the innermost AMR level from the start of the simulation.

The MHD solver employs the local lax-Friedrichs (LLF) Riemann solver to compute the fluxes in the piece-wise linear method (PLM). We initialised a simple uniform magnetic field at $z = 50$ with a value of $B_0 = 0.1 \text{ nG}$ in each direction. We refer the reader to recent work (e.g. Sect. 2.1 in Wittor et al. 2020) for further details on this method. All simulations in this work are non-radiative and only differ in the number and timing of episodes of feedback from SMBH particles.

The jets and relativistic electrons are injected into a galaxy group with a final virial mass of $M_{100} \approx 1.5 \times 10^{14} M_{\odot}$ at $z = 0.0$, $M_{100} \approx 1.1 \times 10^{14} M_{\odot}$ at $z = 0.5$ and $M_{100} \approx 5 \times 10^{13} M_{\odot}$ at $z = 1$. The green colours in Fig. 1 help to visualise its main evolutionary events. At $z = 1$, the group still has to assemble about $2/3$ of its mass, which is later accreted mostly from a group companion merging at $z \sim 0.8$ (from the upper right corner in the panels). Subsequent minor mergers occur across the entire lifetime of the group, while a more prominent second major merger occurs between $z = 0.3$ and $z = 0.1$, following the accretion of a second massive companion (entering from the right in Fig. 1 at a redshift of $z = 0.5$). Throughout this paper, we used the following cosmological parameters: $h = 0.678$, $\Omega_{\Lambda} = 0.692$, $\Omega_{\text{M}} = 0.308$ and $\Omega_{\text{b}} = 0.0478$, based on the results from the Planck Collaboration XIII (2016).

2.2. Modelling the growth of supermassive black holes and radio jets

The simulation of SMBHs follows the formulation by Kim et al. (2011), released in the public version of ENZO and supplemented with a few ad-hoc prescriptions to include the magnetic feedback from radio jets. Given the absence of radiative cooling, our runs lack a self-regulating mechanism to switch the feedback cycle on and off (e.g. Gaspari et al. 2011; Rasia et al. 2015; Ricarte et al. 2019, for a few examples). The thermal structure of the ICM around the SMBH is thus not entirely realistic, which also implies that typical parameters for the launching of jets from AGN must be adjusted to reproduce realistic radio galaxies.

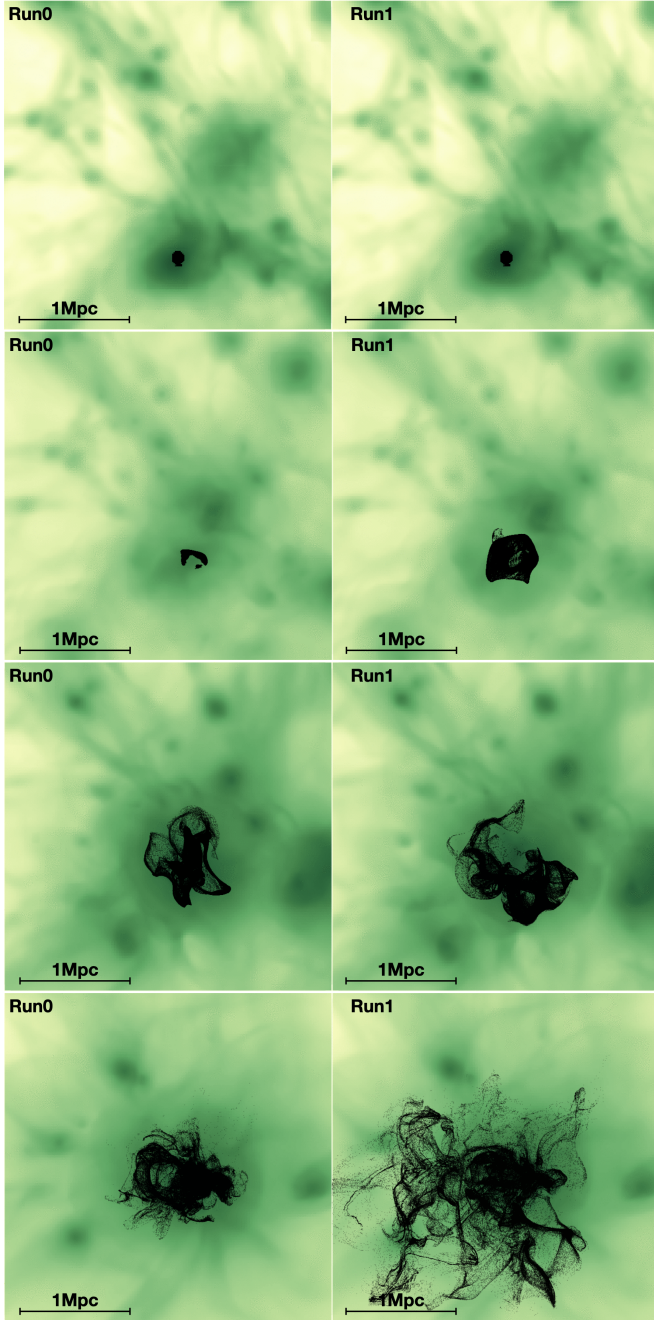


Fig. 1. Maps of all tracers evolved in our run Run0 (*left*) and Run1 (*right*) at $z = 1$, $z = 0.8$, $z = 0.5$, and $z = 0.1$. The colours represent the projected gas density (with a \log_{10} stretching). The line of sight is parallel to the jet axis, to give a sense of the lateral expansion of tracers relative to the jet (which points towards the observer in this case).

After extensive testing of the possibility of generating kinetically dominated jets as implemented in other simulations (Dubois et al. 2010; Gaspari et al. 2011), we resorted to purely thermal energy feedback around the SMBH. This was motivated by the fact that even the interaction of a fast jet with a $T_{\text{ICM}} \geq 10^7$ K cluster core will not produce realistic shock heating and dynamics. This is in conflict with usual models for AGN jets in cool-core atmospheres (where $T \leq 10^6$ K during the jet launching stage; e.g. Brighenti & Mathews 2000; Brüggén & Kaiser 2002). While a pure thermal feedback would also be in conflict with recent Sunyaev-Zeldovich measurements of AGN-blown

cavities that show a substantial amount of non-thermal support inside these cavities (Abdulla et al. 2019), a large fraction of the feedback energy in our model is also provided by the magnetic and kinetic energy produced by our bipolar magnetic feedback model (see below). This approach allowed us to relax the otherwise tight constraint on the time-step in our simulation, set by the typically large jet velocities ($v_j \sim 10^4$ km s $^{-1}$) in the vicinity of the SMBH.

In summary, our approach is suitable to investigate the impact of radio galaxies on the gas in large-scale structures, provided that we focus on $\gg 10$ kpc scales and that dynamical features on smaller scales can be neglected.

Following the implementation by Kim et al. (2011), each SMBH particle is allowed to accrete gas, based on the spherical Bondi-Hoyle model. Due to the lack of spatial resolution, it is necessary to simulate the mass growth of SMBH with ad-hoc parametric formulations. For example, the commonly used Eddington-limited Bondi-Hoyle accretion generally has to be boosted by an efficiency parameter $\alpha \geq 1$, so

$$\dot{M}_{\text{BH}} = \min \left(\frac{4\pi\alpha G^2 M_{\text{BH}}^2 \rho_{\text{B}}}{c_s^3}; \frac{4\pi G M_{\text{BH}} m_{\text{p}}}{\epsilon_{\text{r}} \sigma_{\text{T}} c} \right), \quad (1)$$

where M_{BH} is the SMBH's mass, c_s is the sound speed of the gas at the SMBH's location (which we assume to be relative to a fixed 10^6 K temperature of the accretion disc), ρ_{B} is the local gas density, m_{p} is the proton mass, σ_{T} is the Thomson scattering cross-section, and ϵ_{r} is the radiative efficiency of the SMBH, so $L_{\text{BH}} = \epsilon_{\text{r}} \dot{M}_{\text{BH}} c^2$ is the bolometric luminosity of the SMBH.

Given our resolution, we cannot resolve the Bondi radius and simulate how the SMBH gravitationally influence their surroundings. Neither can we resolve the multi-phase interstellar medium around the host galaxy, given that we do not include cooling and star formation. Hence, we adopted a factor, $\alpha_{\text{Bondi}} > 1$, (e.g. Booth & Schaye 2009; Gaspari et al. 2012; Tremblay et al. 2016) that parametrises the true mass accretion rate onto the SMBH. After testing, we used two different values of α_{Bondi} depending on the epoch of jet injection, which also depends on the spatial resolution at the location of SMBH seed particles. For models in which radio jets start at $z = 1$ (Run1), our computational grid is not fully refined at the location of the SMBHs, which combined with the lack of radiative cooling requires a high value for α , that is $\alpha_{\text{Bondi}} \sim 10^3$ – 10^4 , in order to produce jets leading to a realistic radio morphology. For the simulation in which our radio jets are launched at $z = 0.5$ (Run2), the cluster has largely assembled and the computational grid is refined down to the highest AMR level, at least around the SMBH region. In this case, a modest boost factor ($\alpha_{\text{Bondi}} \sim 5$ – 10) is found to produce a jet morphology comparable to real radio galaxies in a dense atmosphere, as in, for example, Booth & Schaye (2009).

The ENZO model for SMBH feedback by Kim et al. (2011) deposits energy at the maximum numerical resolution in the form of thermal energy. A SMBH particle releases thermal feedback on the surrounding gas, as an extra thermal energy output from each black hole particle, assuming an efficiency $\epsilon_{\text{r}} \epsilon_{\text{BH}} = E_{\text{jet}} / (\Delta M \Delta t c^2)$ between the accreted mass, ΔM , during the timestep (Δt) and the feedback energy E_{jet} . The thermal feedback energy is distributed to the neighbouring 27 gas cells around the SMBH. We assumed ENZO's default efficiency parameters, $\epsilon_{\text{r}} = 0.1$ and $\epsilon_{\text{BH}} = 0.05$ (e.g. Kim et al. 2011; Bryan et al. 2014), which also yielded a good match with observed galaxy clusters scaling relations as found in previous works (Vazza et al. 2013, 2017a).

Table 1. Input parameters for the SMBH models in our simulations and reference parameters for the AGN jets, measured as an average at the end of each jet’s life (t_{jet}).

Parameter	Run2	Run1
z_{jet}	0.5	1.0
$M_{\text{BH}} [M_{\odot}]$	10^9	10^7
α_{Bondi}	10	10^4
$\dot{M}_{\text{BH}} [M_{\odot} \text{ yr}^{-1}]$	10^{-7}	10^{-9}
$t_{\text{jet}} [\text{Myr}]$	10	200
$L_{\text{BH}} [\text{erg s}^{-1}]$	1.7×10^{45}	1.7×10^{44}
$E_{\text{kin,jet}} [\text{erg}]$	2.6×10^{56}	5.6×10^{57}
$E_{\text{th,jet}} [\text{erg}]$	1.2×10^{57}	5.1×10^{57}
$E_{\text{mag,jet}} [\text{erg}]$	1.6×10^{56}	3.7×10^{57}
$B_{\text{av,jet}} [\mu\text{G}]$	1.4	3.6
$B_{\text{max,jet}} [\mu\text{G}]$	3.9	43.2
$v_{\text{av,jet}} [\text{km s}^{-1}]$	630	1267

The SMBHs also inject magnetic fields in the form of magnetic dipoles (2×2 cells at the highest resolution level) located at ± 1 cell along the z -direction from the SMBH). This very simple topology is made necessary by the limitation of spatial resolution. More sophisticated choices, for example considering helical magnetic fields (Ruszkowski et al. 2007), require a higher spatial resolution of ≤ 0.1 kpc (e.g. Candelaresi & Del Sordo 2020). The imposition of a fixed jet alignment along the z axis is not very physical. Yet, the jets are launched only once and the simulation lacks physical and spatial details in the gas accretion onto the SMBH. Hence, any launching direction seems equally likely, and therefore we pre-defined a fixed launching axis in order to make the post-processing analysis easier.

The injected magnetic energy is normalised to a fixed fraction of the total feedback energy $E_{\text{B,jet}} = \epsilon_{\text{B,jet}} E_{\text{jet}}$, with $\epsilon_{\text{B,jet}} = 0.1$. However, this does not directly correspond to the magnetisation of jets since the thermal energy is released isotropically around the SMBH, while the magnetic energy is directed along a specific direction². For this reason, the typical magnetic energy of our jets (see e.g. Table 1) is a factor of ~ 10 higher than the kinetic and thermal energy assigned to cells at the poles of SMBHs, where jets are launched, making them initially magnetically dominated (e.g. Xu et al. 2009; Massaglia et al. 2019).

In this work, we restrict our discussion to the results of three runs, and in particular of two different combinations of feedback parameters (beside the reference simulation without jets), which produce plausible radio jet morphologies at $z \sim 1$ (Run1) and at $z \sim 0.5$ (Run2). The kinetic jet power of these two runs is across the $\sim 10^{45}$ erg s⁻¹ border, which based on correlations derived by radio surveys (e.g. Turner & Shabala 2015; Vardoulaki et al. 2021) can be turned into a $L_{1.4} \sim 10^{25}$ W Hz⁻¹ luminosity, thus across the standard FR-radio dicotomy. Therefore, our two runs can be seen as a first exploration of the propagation of fossil electrons ejected by FRI (Run1) and FRII (Run2) radio galaxies, respectively, in a poor group and in a more massive and evolved version of the same system.

A more extensive survey of the effect of physical relevant variations of feedback parameters (e.g. α_{Bondi} , $\epsilon_{\text{B,jet}}$, ϵ_r , etc.), as well as on the impact of multiple or restarted jets within the same

galaxy group will be the subject of a follow-up campaign of simulations.

In summary, the scenarios we explored in this work are: (a) Run0: No SMBH feedback is activated. This simulation is essentially a standard non-radiative MHD simulation, in which the ICM magnetic fields are the result of compression and (partly) small-scale dynamo amplification of the initial $B_0 = 0.1$ nG seed field³. (b) Run1: In this case, the SMBH at the centre of the most massive halo in the high-resolution region is activated at redshift $z = 1$, has an initial mass of $M_{\text{BH}} = 10^7 M_{\odot}$, and remains active for ≈ 200 Myr, releasing its thermal and magnetic feedback into the ICM. We set $\alpha_{\text{Bondi}} = 10^4$ to boost the accretion rate. The initial magnetic seed field is the same as in Run0. Hence, the magnetisation of the ICM is the combined result of seed field amplification and AGN feedback. (c) Run2: This is the same as in Run0 until $z = 0.5$, and then a $M_{\text{BH}} = 10^9 M_{\odot}$ SMBH is placed at the centre of the most massive halo in the high-resolution region (which is inside an already formed galaxy group). The SMBH releases thermal and magnetic feedback for ≈ 10 Myr. As in Run1, the magnetisation of the ICM stems from the combination of seed field amplification and AGN feedback. In this case, we use $\alpha_{\text{Bondi}} = 10$ to boost the (unresolved) mass accretion rate onto the SMBH. The initial magnetic seed field is the same as in Run0.

Table 1 gives more details of the list of parameters describing the jet launching in all runs. These are measured within the jet volume, after a time t_{jet} . Possible caveats of our method are discussed in Sect. 4.

2.3. CRaTer simulations of Lagrangian tracer particles

We use the Lagrangian code CRaTer to follow the spatial evolution of the cosmic-ray electrons in our runs. In previous work, CRaTer has been used to study cosmic rays and turbulence in galaxy clusters (e.g. Wittor et al. 2016, 2017a,b). For details of the implementation, we invite the reader to consult the references stated in parentheses.

In post-processing, we injected $\sim 2 \times 10^6$ particles in all runs, starting from the highest-density peaks of the simulation at $z = 1$ in Run1 (and Run0) and $z = 0.5$ in Run2 (and Run0), with a mass resolution $m_{\text{trac}} = 5 \times 10^5 M_{\odot}$, and we evolved them using all snapshots of the simulation (~ 120 for Run1 and ~ 100 for Run2). The various grid quantities, such as density and velocity, are assigned to the tracers using a cloud-in-cell (CIC) interpolation method. Further details on the full procedure implemented to advect tracers in our simulations, in order to properly sample the advection of gas matter performed by the ENZO (Eulerian) calculation, we refer the reader to Wittor (2017) and Wittor et al. (2016).

Figure 1 shows the spatial evolution of all tracers in runs Run0 and Run1, where tracers were initialised at $z = 1$. The maps are projected along the jet axis to show the dispersal of tracers in directions perpendicular to the jets. Although the large-scale dynamics of the cluster is the same in both runs, the impulsive feedback from the radio galaxy, even with a single event, appears to increase the filling factor of tracer particles as a function of time (a longer discussion can be found in Sect. 3.3).

³ In comparison with our most resolved simulations in Vazza et al. (2018) and Domínguez-Fernández et al. (2019), the fraction of volume where the Alfvén scale is well resolved is smaller, owing to the less aggressive AMR strategy employed here. Hence, small-scale dynamo amplification can only develop in a smaller volume.

² We note that we systematically oriented the poles along the same coordinate axis.

While all tracers (also in Fig. 8) were injected at the highest density peaks, only $\sim 10^5$ tracers were used to compute the radio spectra. Those tracers were selected based on the values of magnetic field strength ($\geq 10 \mu\text{G}$) and the magnitude of the velocity with respect to the SMBH ($|v| \geq 600 \text{ km s}^{-1}$) at the moment of the first injection of AGN jets, so that only the gas directly entrained by jets is initially enriched with cosmic rays.

After their injection, we used a temperature-jump-based shock finder to detect when tracer particles encounter a shock (Sect. 2.2 in Wittor et al. 2017a). For each detected shock, they compute the Mach number according to

$$M = \sqrt{\frac{4}{5} \frac{T_{\text{new}} \rho_{\text{new}}}{T_{\text{old}} \rho_{\text{old}}} + \frac{1}{5}}. \quad (2)$$

Our tracer particles also keep track of the local fluid divergence, $\nabla \cdot \mathbf{v}$, and of the fluid vorticity, $\nabla \times \mathbf{v}$, which serve as proxies for the local turbulence experienced by the tracer particles. Hence, we can estimate the effects of compression or rarefaction as well as turbulent re-acceleration on the electron energy distribution (Sect. 2.4). In particular, we used the gas vorticity to estimate the solenoidal turbulence experienced by particles, $\sigma_v = |\nabla \times \mathbf{v}| l_{\text{scale}}$, where for simplicity we used the same fixed reference scale of $l_{\text{scale}} = 27 \text{ kpc}$ used to compute vorticity via finite differences (i.e. three cells on the high-resolution mesh). The vorticity is used to compute the turbulent re-acceleration model outlined below, as well as the (solenoidal) turbulent kinetic energy flux. In our model for turbulent re-acceleration (Sect. 2.4) the kinetic energy flux is the key input. We assume that this is constant across the Kolmogorov turbulent cascade, provided the turbulence injection scale is always $\geq l_{\text{scale}}$. The assumption of a turbulent cascade close to a Kolmogorov model, and of an injection scale $\geq 27 \text{ kpc}$ is supported by our previous simulations of turbulence in the ICM (e.g. Vazza et al. 2017b; Wittor et al. 2017b; Angelinelli et al. 2020). For more recent applications of passive tracers to study the evolution of cosmic rays in galaxy clusters or turbulence in the ICM, we refer the reader to Wittor et al. (2020) and Wittor & Gaspari (2020).

2.4. Simulating the evolution of electron spectra

We solve the time-dependent diffusion-loss equation of relativistic electrons represented by tracer particles using the standard Chang & Cooper (1970) finite-difference scheme, which is implemented in the programming language Julia⁴. We typically used $N_b = 4000$ equal energy bins in the $p_{\text{min}} \leq p \leq p_{\text{max}}$ momentum range (with $P = \gamma m_e v$ and $p = P/(m_e c)$ being the normalised momentum of electrons and $p_{\text{min}} = 1$ and $p_{\text{max}} = 2 \times 10^4$; hence, $dp = 5$).

Considering the reduced Fokker-Planck equation without injection and escape terms (i.e. Liouville equation), the evolution of the number density of relativistic electrons as a function of momentum $N(p)$ can be computed separately for each tracer particle:

$$\frac{\partial N}{\partial t} = \frac{\partial}{\partial p} \left[N \left(\left| \frac{p}{\tau_{\text{rad}}} \right| + \left| \frac{p}{\tau_{\text{c}}} \right| + \frac{p}{\tau_{\text{adv}}} - \left| \frac{p}{\tau_{\text{acc}}} \right| \right) \right] + \frac{\partial^2}{\partial p^2} (D_{\text{pp}} N), \quad (3)$$

where D_{pp} is the particle diffusion coefficient in momentum space. We can thus define

$$\dot{p} \approx \left| \frac{p}{\tau_{\text{rad}}} \right| + \left| \frac{p}{\tau_{\text{c}}} \right| + \frac{p}{\tau_{\text{adv}}} - \left| \frac{p}{\tau_{\text{acc}}} \right|. \quad (4)$$

⁴ <https://julialang.org>

In the following, we neglect the stochastic term, D_{pp} . In Eq. (3), the numerical solution is obtained with the Chang & Cooper (1970) finite difference scheme:

$$N(p, t + dt) = \frac{N(p, t)/dt + N(p + dp, t + dt)p}{1/dt + p/dp} + Q_{\text{inj}}, \quad (5)$$

where in the splitting-scheme for finite differences we assumed $N(p + dp/2) = N(p + dp)$ and $N(p - dp/2) = N(p)$, and Q_{inj} accounts for the injection by radio galaxies or shocks, whenever present, regarded as an instantaneous process owing to the timescales being much shorter than the time step of our integration (see Eq. (12) below).

With this simple approach to solve Fokker-Planck equations, we can only model the systematic acceleration by turbulent re-acceleration. In order to model the stochastic acceleration, which can lead to higher electron energies, one has to resort to more complex solvers (e.g. Donnert & Brunetti 2014, for an application to numerical simulations).

In order to quantify the effects of different mechanisms on the observed properties of radio emission, we compare the outcome of three models applied to our simulated electron evolution: (a) a model in which relativistic electrons are injected by radio jets (assuming an initially unbroken power-law energy distribution with slope $\delta_r = -2.0$) and subsequently only subject to energy losses as they are advected in the ICM; (b) a model in which, beside the injection of relativistic electrons by jets and their continuous cooling during advection, new relativistic electrons can be injected at shock waves (via the Q_{inj} term in Eq. (5)), as well as by considering the re-acceleration by weak shocks ($\mathcal{M} \leq 3$); (c) a model in which, beside the two acceleration mechanisms considered above and the continuous cooling, electrons can also be re-accelerated by the turbulent re-acceleration via second-order acceleration (Eq. (17)).

By comparing the radio properties of cosmic-ray electrons in these three models, we infer the most likely distribution of fossil electrons, injected by radio galaxies. The main routines to solve for the evolution of relativistic electrons are written and parallelised in the Julia (v1.4.0) language. This allows us to simultaneously evolve three different realisations of the momentum spectra over $N_b = 4000$ bins for $\sim 10^5$ tracers with ~ 100 s/step, using 16 threads on eight Intel I9 cores⁵.

2.4.1. Loss terms

The loss timescales for the radiative, Coulomb, and expansion (compression) processes are given by the following formulae, adapted from Brunetti & Jones (2014):

$$\tau_{\text{rad}} = \frac{7720 \text{ Myr}}{(\gamma/300) \left[\left(\frac{B}{3.25 \mu\text{G}} \right)^2 + (1+z)^4 \right]}, \quad (6)$$

$$\tau_{\text{c}} = 7934 \text{ Myr} \left\{ \frac{n/10^{-3}}{\gamma/300} \left(1.168 + \frac{1}{75} \ln \left(\frac{\gamma/300}{n/10^{-3}} \right) \right) \right\}^{-1}, \quad (7)$$

and

$$\tau_{\text{adv}} = \frac{951 \text{ Myr}}{\nabla \cdot \mathbf{v} / 10^{-16}}, \quad (8)$$

⁵ A serial version of the code, containing all of the most important features and a sample sequence of tracer particle data is publicly available here: https://github.com/FrancoVazza/JULIA/tree/master/CR_solver_pub.

where n is measured in $[\text{cm}^{-3}]$, B in $[\mu\text{G}]$, and $\nabla \cdot \mathbf{v}$ in $[1/s]$. We neglect bremsstrahlung losses since their timescale is significantly longer than the ones of all other loss channels for the ICM physical condition considered here.

2.4.2. Gain terms – shock acceleration

Concerning energy gains for relativistic electrons, we considered the contribution from Fermi-I-type acceleration from shocks (i.e. via diffusive shock acceleration) and from Fermi-II-type acceleration (i.e. from adiabatic-stochastic acceleration). The shock kinetic energy flux that is converted into the acceleration of cosmic rays (e.g. [Ryu et al. 2003](#)) is given by

$$\Psi_{\text{CR}} = \xi_e \eta(\mathcal{M}) \frac{\rho_u V_s^3 dx_t^2}{2}, \quad (9)$$

where ρ_u is the pre-shock gas density, V_s is the shock velocity, and the combination $\xi_e \eta(\mathcal{M})$ gives the cosmic-ray acceleration efficiency. This comprises a prescription for the energy going into cosmic rays, $\eta(\mathcal{M})$, and the ratio of acceleration rates of electrons to that of protons, ξ_e . For convenience of implementation, we used the polynomial approximation given by [Kang & Jones \(2007\)](#) for $\eta(\mathcal{M})$, which includes the effects of finite Alfvén wave drift and wave energy dissipation in the shock precursor. dx_t^2 is the surface associated with each of the tracers, which we can compute considering that $dx_t^3 = dx^3/n_{\text{tracers}}$ is the initial volume associated with every tracer at the epoch of their injection (n_{tracer} being the number of tracers in every cell), and $dx_t(z)^3 = dx^3 \cdot \rho_t/\rho(z)$ is the relative change of the volume associated with each tracer as a function of z , based on the ratio between the density at injection, ρ and the density of cells where each tracer sits as a function of redshift, $\rho(z)$.

For the electron-to-proton ratio, $\xi_e \sim 10^{-2}$ would be commonly used to model strong supernova remnant shocks (e.g. [Uchiyama et al. 2007](#)). However, the exact ratio is extremely uncertain for weak shocks, and several sophisticated particle-in-cell simulations have been performed in recent years to investigate this (e.g. [Riquelme & Spitkovsky 2011](#); [Guo et al. 2014a,b](#); [Xu et al. 2020](#)). In order to compare to previous work on fossil electrons, we followed the previous work by [Pinzke et al. \(2013\)](#) strictly and linked the injection of fresh electrons to the possible one protons injected by diffusive shock acceleration (DSA), by requiring an equal number density of cosmic-ray electrons and protons above a fixed injection momentum, which yields $\xi_e = (m_p/m_e)^{(1-\delta_{\text{inj}})/2}$. This approach gives $\xi_e \sim 10^{-2}$ for an injection spectral index of $\delta_{\text{inj}} \approx 2.3$, in line with the injection spectral index of local Galactic supernova remnants. For simplicity, we also neglect a possible dependence of the shock acceleration efficiency on the local magnetic field topology, which could change the cosmic ray content of galaxy clusters (e.g. [Wittor et al. 2020](#); [Banfi et al. 2020](#); [Guo et al. 2014a](#); [Xie et al. 2020](#)).

Following the DSA thermal leakage model, we assume that the injection momentum P_{inj} is a multiple of the thermal momentum of particles, that is $P_{\text{inj}} = \xi P_{\text{th}}$ ($P_{\text{th}} = \sqrt{2k_b T_d m_p}$). Here, we obtain ξ based on the fit formula provided by [Kang & Ryu \(2011\)](#) for their one-dimensional convection-diffusion simulations:

$$\xi = 1.17 \frac{m_p v_d}{\rho_{\text{th}}} \cdot \left(1 + \frac{1.07}{\epsilon_B}\right) \left(\frac{\mathcal{M}}{3}\right)^{0.1}, \quad (10)$$

in which v_d is the downstream shock velocity and ϵ_B is the ratio between the downstream magnetic field strength (B_0) generated

by the shock, and it is the large scale magnetic field perpendicular to the shock normal (B_{\perp}). We fixed $\epsilon_B = 0.23$, consistently with [Pinzke et al. \(2013\)](#), which gives an injection parameter $\xi \sim 2.5\text{--}3.5$ for the shocks in our simulation.

We inject relativistic electrons with a momentum distribution that follows a power law (e.g. [Kardashev 1962](#); [Sarazin 1999](#)):

$$Q_{\text{inj}}(p) = K_{\text{inj}} p^{-\delta_{\text{inj}}} \left(1 - \frac{p}{p_{\text{cut}}}\right)^{\delta_{\text{inj}}-2}, \quad (11)$$

in which the initial slope of the input momentum spectrum, δ_{inj} , follows from the standard DSA prediction, $\delta_{\text{inj}} = 2(\mathcal{M}^2 + 1)/(\mathcal{M}^2 - 1)$. p_{cut} is the cut-off momentum, which is defined for every shocked tracer as the maximum momentum, beyond which point the radiative cooling timescale becomes shorter than the acceleration timescale, τ_{DSA} :

$$\tau_{\text{DSA}} = \frac{3 D(E)}{V_s^2} \cdot \frac{r(r+1)}{r-1}, \quad (12)$$

where r is the shock compression factor and $D(E)$ is the electron diffusion coefficient as a function of energy (e.g. [Gabici & Blasi 2003](#)). The specific energy-dependent value of $D(E)$ is poorly constrained and it depends on the local turbulent conditions of the plasma undergoing shocks. It is however critical to set the maximum energy that can be reached by shock acceleration (e.g. [Kang et al. 2012](#)). Nevertheless, this is not an issue for our work, as all plausible choices of $D(E)$ in Eq. (12) give an acceleration timescale that is many orders of magnitude smaller than the typical cooling time of radio emitting electrons, whose momentum distribution at injection can be assumed to follow a power law within our momentum range of interest.

This also motivates the fact that we can model DSA shock injection by adding the newly created population of particles across time steps (see Eq. (5) below), without integrating a source term as is needed for the much slower re-acceleration by turbulence (see below).

The expression for the normalisation factor, K , can thus be derived by equating the cosmic-ray energy flux crossing each tracer volume element, and the product between the total energy of cosmic rays advected with a post-shock velocity (v_d):

$$\Psi_{\text{CR}} dx_t = v_d E_{\text{CR}}, \quad (13)$$

where v_d is the downstream (post-shock) velocity

$$E_{\text{CR}} = \int_{p_{\text{inj}}}^{p_{\text{cut}}} Q_{\text{inj}}(p) T(p) dp, \quad (14)$$

with $Q_{\text{inj}}(p)$ defined as above and $T(p) = (\sqrt{1+p^2} - 1)m_e c^2$. The integration yields (e.g. [Pinzke et al. 2013](#))

$$E_{\text{CR}} = \frac{K_{\text{inj}} m_e c^2}{\delta_{\text{inj}} - 1} \left[\frac{B_x}{2} \left(\frac{\delta_{\text{inj}} - 2}{2}, \frac{3 - \delta_{\text{inj}}}{2} \right) + p_{\text{cut}}^{1-\delta_{\text{inj}}} \left(\sqrt{1 + p_{\text{cut}}^2} - 1 \right) \right], \quad (15)$$

where $B_x(a, b)$ is the incomplete Bessel function and $x = 1/(1 + p_{\text{cut}}^2)$.

2.4.3. Gain terms – shock re-acceleration

Besides the direct injection of relativistic electrons by shocks, we also include re-acceleration by shocks waves (e.g.

Markevitch et al. 2005; Kang & Ryu 2011; Kang et al. 2012). According to DSA, the input particle spectrum, $N_0(x)$, becomes

$$N(p) = (\delta + 2) \cdot p^{-\delta} \int_{p_{\min}}^p N_0(x) x^{\delta+1} dx, \quad (16)$$

where δ is the slope corresponding to the new shock, according to DSA.

2.4.4. Gain terms – turbulent re-acceleration

Turbulence is thought to play a major role in producing giant radio halos in galaxy clusters, in connection with mergers (e.g. Brunetti & Jones 2014, and references therein). Some residual level of turbulence is expected to be present at all times (e.g. Vazza et al. 2011; Angelinelli et al. 2020); it is caused by minor mergers (e.g. Norman & Bryan 1999; Cassano & Brunetti 2005; Iapichino & Niemeyer 2008; Wittor et al. 2017a), AGN feedback (e.g. Gaspari et al. 2011; Bourne & Sijacki 2021), and cool core sloshing (e.g. ZuHone et al. 2010). The solenoidal component of turbulence is prominent in clusters (e.g. Miniati 2014; Vazza et al. 2017b). According to Brunetti & Lazarian (2016), solenoidal turbulence can re-accelerate particles via stochastic interaction with diffusing magnetic field lines in super-Alfvénic turbulence developed in the ICM. In addition to radio halos, this mechanism has also been used in models of γ -ray bursts (Xu & Zhang 2017) and radio bridges between galaxy clusters (Brunetti & Vazza 2020; Bonafede et al. 2021). The implied acceleration timescale is thus

$$\tau_{\text{ASA}} = \frac{p^2}{4D_{\text{pp}}} = 1.25 \times 10^5 \text{ Myr} \frac{L/(0.5) B}{\sqrt{n/10^{-3}} (\delta V/10^7)^3}, \quad (17)$$

where L is measured in Mpc and δV is the local gas turbulent velocity within the scale L , measured in centimeters per second. Based on this formula, it can be seen that for typical ICM conditions, only for (solenoidal) turbulent rms velocities of $\delta V \geq 300 \text{ km s}^{-1}$ can this mechanism produce acceleration on timescales of $\leq \text{Gyr}$ (e.g. Sect. 3.4).

The interaction between particles and turbulence is a stochastic process that can be thought of as the combination of two effects. Firstly, electrons are systematically accelerated on a timescale given by Eq. (17), and, secondly, their energy is changed stochastically (Eq. (3)). Starting from a mono-energetic initial distribution of electrons, these two effects result in the progressive widening of the momentum distribution of electrons, with a median value determined by the systematic acceleration (captured by our solver).

2.4.5. Injection of electron by jets

Finally, the injection of relativistic electrons from radio galaxies assumes that a new population of electrons is generated at each tracer located in a jet-launching cell, as

$$K_r \int_{p_{\min}}^{p_{\max}} p^{-\delta_r} dp = \phi_e m_{\text{trac}}, \quad (18)$$

where we assume an injection spectrum of $\delta_r = 2$, and we set ϕ_e so that the number of all injected relativistic electrons is 10^{-3} of the total number of thermal electrons for each tracer, meaning a few $\sim 10^{-7} \text{ part cm}^{-3}$ (e.g. Mendygral et al. 2012).

3. Results

Using cosmological MHD simulations, we addressed the following questions: what is the impact of jets from radio galaxies on the thermodynamic, kinematic, and magnetic properties of the ICM? How much do these effects influence the distribution of relativistic electrons in the ICM? How do the properties of relativistic electrons change depending on loss and (re)acceleration mechanisms arising from the interaction with the ICM?

In the following sections, we discuss each of these questions with regard to our results.

3.1. Radio source evolution

Radio galaxies have historically been separated into two classes based on the radio surface brightness of their cocoons (Fanaroff & Riley 1974). While Fanaroff & Riley type II (FR II) sources show well-defined jet termination shocks around edge-brightened cocoons, type I sources (FR I) have peaks of surface brightness closer to the core. Both classes of FR sources are thought to initially expand supersonically, with the jet-environment interaction likely to have a decisive role in determining when FR II sources evolve into FR I systems, following the disruption of their jets (e.g. Kaiser & Alexander 1997; Turner & Shabala 2015). Moreover, many radio sources associated with low- z galaxies and detected by recent surveys are compact and small in size, and they can be regarded as one of the extremes (FR 0) of a continuous population of radio galaxies, with a broad distribution of sizes and luminosities (e.g. Capetti et al. 2019; see, however, Hardcastle & Croston 2020 for a different take on FR 0 sources).

Our simulated radio sources appear to have broad morphological similarity with FR II-type sources, but in both cases they show a dynamic evolution. Figures 2 and 3 show the evolution of radio emission (at 50 MHz) in the first evolutionary stages ($\leq 400 \text{ Myr}$) of radio galaxies in the two runs, where we numerically integrated the synchrotron emission from each tracer assuming the Jaffe Perola ageing model (Jaffe & Perola 1973). The frequencies used to compute the emission in this work are the ‘LOFAR’ frequencies of 50 and 140 MHz and the ‘JVLA’ frequency of 1400 MHz. The typical total emission power at 140 MHz of each radio jet is of several $\sim 10^{35} \text{ erg s}^{-1} \text{ Hz}^{-1}$ 100 Myr after their injection, and it fades to $\leq 10^{33} - 10^{34} \text{ erg s}^{-1} \text{ Hz}^{-1}$ 200 Myr after injection, due to the combination of radiative cooling and adiabatic losses experienced by lobes.

Jets in Run2 are quickly distorted and bent by the interaction with the surrounding turbulent ICM, while they remain more collimated in Run1, owing to the lower and narrower amplitude of the pressure profile of the gas atmosphere in the cluster at $z \sim 1$. Additional renderings for the entire evolution of Run1 and Run2 are shown in the appendix.

Based on their appearance over $\sim 100 - 200 \text{ Myr}$ from the injection of jets, both sources resemble FR II-type galaxies. However, an analysis of the distance of the radio emission peak from the jet core (e.g. Vardoulaki et al. 2019; Mingo et al. 2019) suggests that Run1 source is an FR I galaxy in a fraction of its evolution. However, in the absence of dominant relativistic components in our simulated jets, our model cannot reproduce hot spots of real radio sources.

3.2. The impact of radio galaxies on the ICM

We start by focusing on the dynamics of the ICM as a results of radio galaxies launched at two different times. In Figs. 4 and 5,



Fig. 2. Evolution from $z = 0.49$ to $z = 0.39$ of the radio emission (50 MHz) from jets in our Run2. The red contours (spaced in the square root of the emission) are drawn to better visualise the location of emission peaks in the jet structure. The colour bar gives the emitted power per pixel ($=8.86$ kpc co-moving).



Fig. 3. Evolution from $z = 0.99$ to $z = 0.89$ of the radio emission (50 MHz) from jets in our Run1. The red contours (spaced in the square root of the emission) are drawn to better visualise the location of emission peaks in the jet structure. The colour bar gives the emitted power per pixel ($=8.86$ kpc co-moving).

we show the evolution of the X-ray emission (colours) overlaid with the projected distribution of radio emission at 50 MHz from our tracers (contour) for the two runs. In both cases, no observational cuts were applied in drawing the radio contours. Altogether, we show six snapshots to display the most salient features of AGN feedback: (i) the release of powerful shocks ahead of jets (with $M \sim 3.0$ in Run2 and $M \sim 4.0$ in Run1), marked by discontinuities in the X-ray surface brightness in the first panel of each figure; (ii) the formation of pairs of cavities, partially void of X-ray-emitting gas in the region inflated by the two radio jets (second and third panels of each figure); (iii) in the Run2 case, the development of two ~ 100 – 250 kpc long jets, which remain straight for at least ~ 400 Myr after their ejection; in the Run1 case, jets are already dissolved at ~ 200 Myr after their ejection; (iv) the subsequent evolution of jet-inflated radio lobes, which expand laterally (i.e. perpendicular to the jet axis) up to ~ 300 – 500 kpc; (v) the progressive mixing of the radio-emitting plasma with the ICM, which covers an increasingly larger number of cells in the innermost cluster regions. While

in Run2 the distribution of electrons has a large covering factor in the innermost cluster regions down to $z = 0.1$ (or below), electrons released in Run1 have a much lower covering factor by the end of the simulation. The reason is that they were dispersed in the ICM earlier (last panel).

Next, we investigate the impact of radio galaxies on the radial profiles of gas density, temperature, and magnetic field strength of the ICM. Figure 6 shows the sequence of radial profiles of gas density, temperature, and magnetic field strength comparing Run2 and Run0. The impact of the radio galaxy on the overall properties of the ICM is far from dramatic in these runs. The differences in Run0 models are limited to quite localised excesses of gas heating due to the thermal feedback by AGN-driven shock waves, and to slightly more pronounced excesses of magnetic fields due to radio jets. However, while the differences are clear close to the epoch of jet launching ($z \geq 0.46$), they tend to decrease with time at most radii. However, some excess magnetisation in Run2 (of order ~ 3 – 10) remains visible in the radial profile of the cluster even at a later redshift,

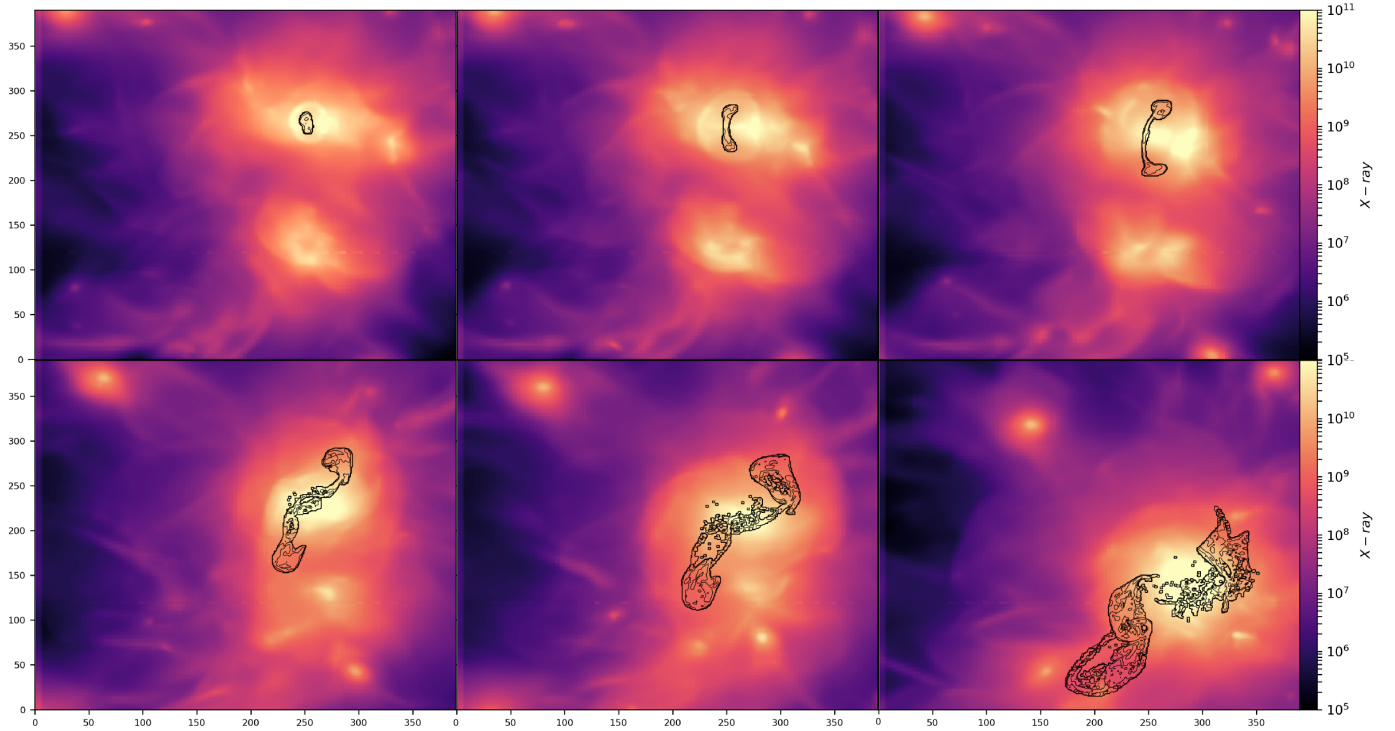


Fig. 4. Evolution of X-ray emission and radio emission (\log_{10} contours) for the Run2 model, in which a radio galaxy is activated at $z = 0.5$. The epochs in the panels are $z = 0.49$, $z = 0.46$, $z = 0.45$, $z = 0.37$, $z = 0.31$, and $z = 0.16$. No observational cut is applied to the maps, and the radio data have been smoothed to a $\times 3$ coarser resolution to allow a better visualisation of contours. The coordinates of each axis are in units of cells ($\delta x = 8.86$ kpc).

within ≤ 250 kpc. Very similar trends are found when comparing the radial profiles of Run1 and Run0 (not shown).

As a caveat, we should stress that our limited (and typically decreasing with radius) spatial resolution prevents the Reynolds number from getting large enough for an efficient amplification of magnetic fields seeded by radio galaxies, which can proceed only when the spatial resolution of the simulation is enough to resolve the Alfvén length scale (e.g. [Donnert et al. 2018](#); [Brunetti & Vazza 2020](#), and references therein). Hence, these simulations likely provide a lower limit to the ICM magnetic field strength after the jet activity has ceased, and future higher resolution (and more expensive) simulations will be needed to assess the maximal possible amplification here. However, recent simulations by [Ehlert et al. \(2021\)](#) support the fact that magnetic fields injected by jets only affect the close proximity of AGN, while the cluster-wide magnetic field distribution is dominated by large-scale turbulence.

3.3. Long-term evolution of relativistic electrons injected by radio galaxies

We now focus on the properties of the ICM as viewed by the tracer particles as they move through the ICM. Figure 7 gives the evolution of the distance travelled by tracers, in which we compared the median distance covered by tracer particles initially placed in jets (or in corresponding cells, in Run0 models). Tracers ejected by radio jets always travel a greater distance compared to their corresponding particles in Run0 models. This follows on from the combined effect of outflows, as well as that of large-scale mixing by turbulent motions, which are typically found to be significant at large radii (e.g. [Angelinelli et al. 2020](#)). The effect is more significant in Run1, where the jet power is

great enough to propel a fraction of the lobe to beyond the cluster virial radius, and in general is sufficient to spread the jet’s material over the entire cluster volume. In Run2, the jets are not powerful enough to escape through the denser and hotter ICM, and the jet material settles at a similar distance as the Run0 case over time. In both jet simulations, being dominated by the fast bipolar transport, the average spatial separation of tracers is faster than a Richardson ($\propto t^{3/2}$) diffusion, which applies to the pair dispersion statistics of passive tracers in Kolmogorov-type turbulence (e.g. [Vazza et al. 2010](#)). The latter trend is instead measured initially in the pair-dispersion statistics of tracers in Run0. Later ($\geq 1-2$ Gyr), the average separation progresses more slowly with time, following normal diffusion ($\propto t^{1/2}$), approximately after tracers have travelled a distance greater than the typical size of turbulent eddies. Interestingly, tracers ejected at $z = 1$, as in Run1, continue to spread in the volume at a relatively fast rate compared to Run2, owing to the fact that their initially faster expansion has placed them (on average) in outer cluster regions, where the mixing due to turbulence and bulk motions is more significant ([Lau et al. 2009](#); [Angelinelli et al. 2020](#)).

The various panels in Fig. 8 show the evolution of magnetic field strength, temperature, and velocity curl for tracers in the various runs. Since tracers in Run2 and Run1 typically spread to a larger radius (and a lower density) compared to the corresponding tracers in the control run (Run0), in this case we always measure the quantities for tracers found within the same radius of the cluster centre (≤ 500 kpc) at all times. The changes of the ambient medium that tracer particles are subjected to are typically violent and involve velocity fluctuations with amplitudes of approximately several hundreds of kilometres per second, even during the later stages of lobe evolution. Figures 9 and 10 show the evolution of the absolute velocity and the

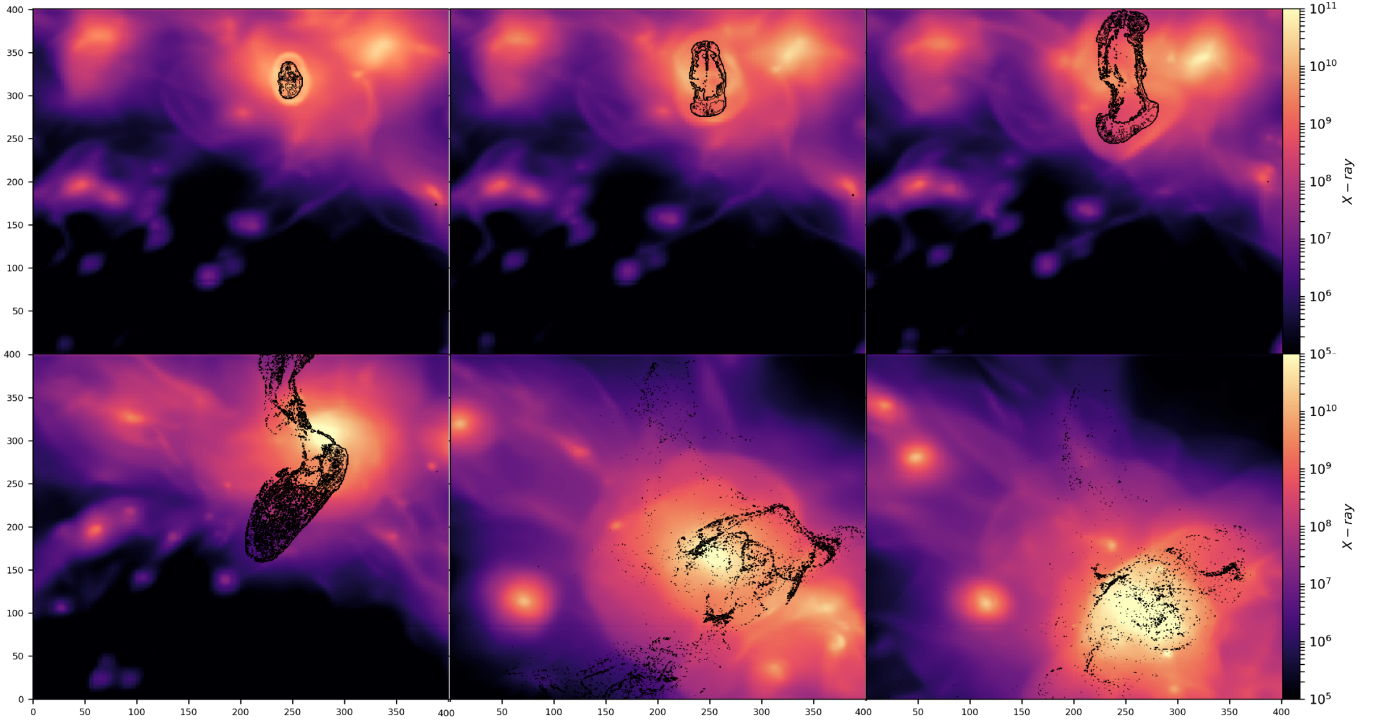


Fig. 5. Evolution of X-ray emission and radio emission (\log_{10} contours) for the Run1 model, in which a radio galaxy is activated at $z = 1.0$. The epochs in the panels are $z = 0.96$, $z = 0.93$, $z = 0.89$, $z = 0.76$, $z = 0.37$, and $z = 0.19$. No observational cut is applied to the maps, and the radio data have been smoothed to a $\times 3$ coarser resolution to allow a better visualisation of contours. The coordinates of each axis are in units of cells ($\delta x = 8.86$ kpc).

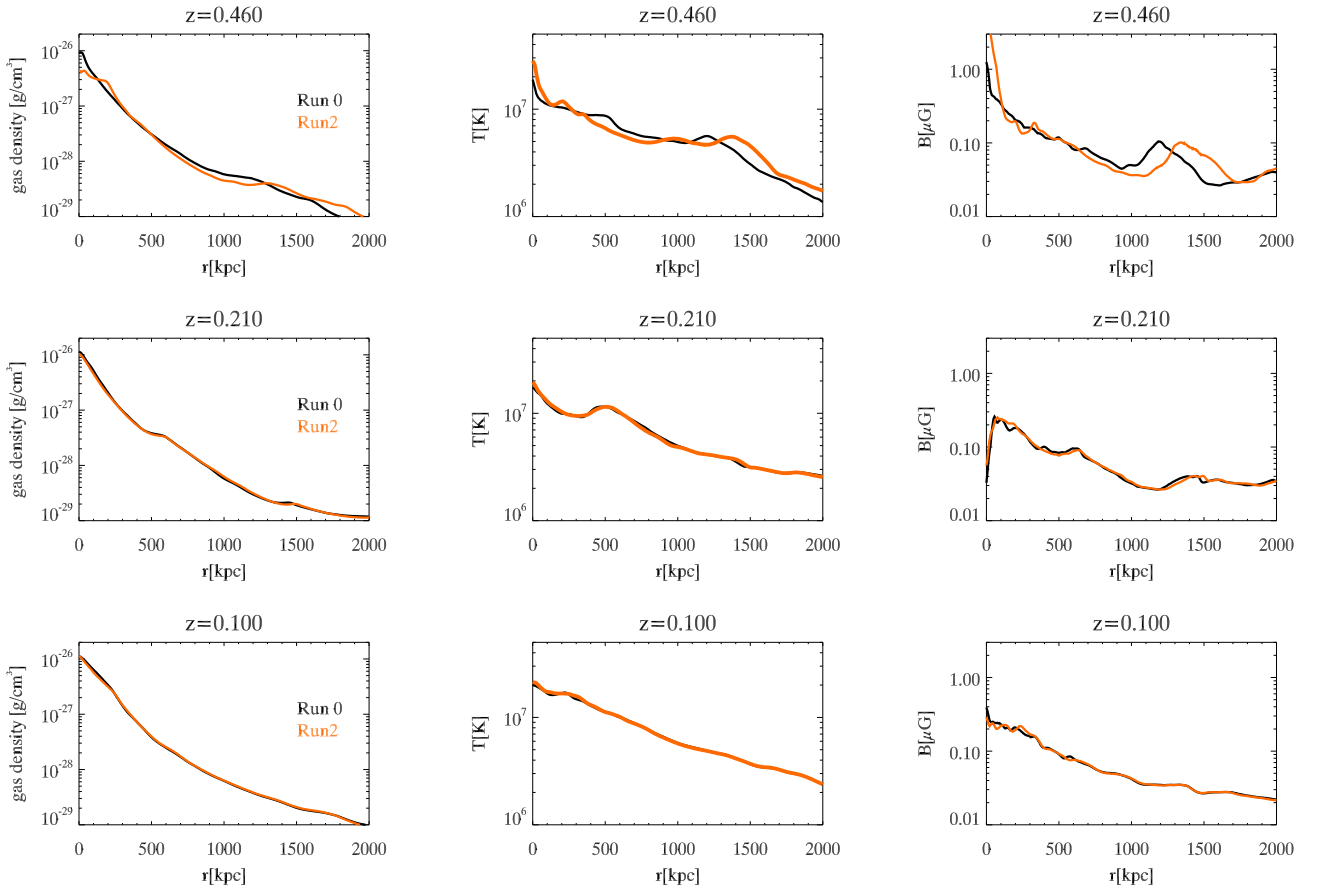


Fig. 6. Radial (mass-weighted) profiles of gas density, gas temperature, and proper magnetic field strength for Run0 and Run2 at three different epochs.

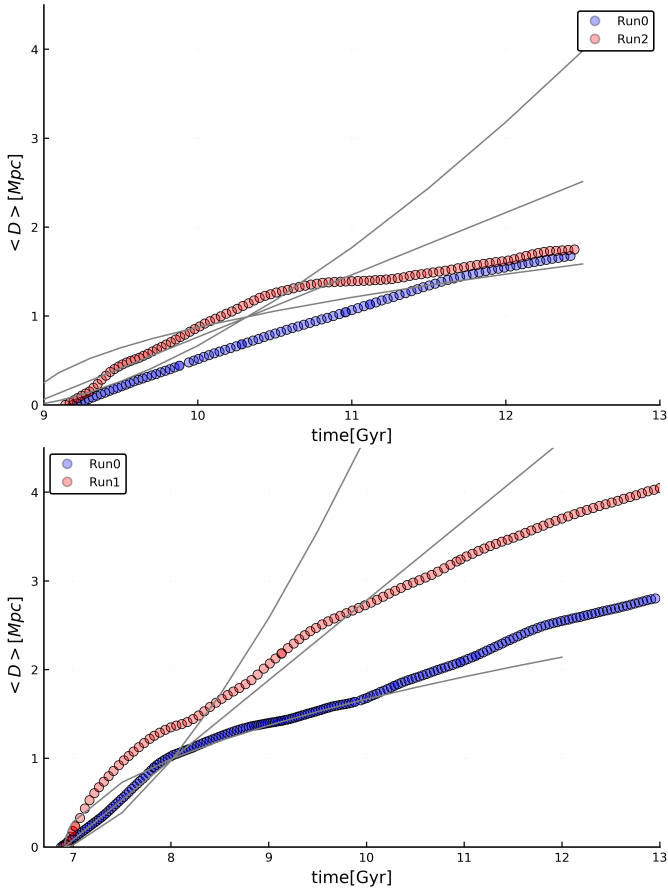


Fig. 7. Evolution of the median distance (in co-moving Mpc) covered by tracers since their initial injection in our runs as a function of time for Run2 versus Run0 (*top*, injection at $z = 0.5$) and for Run1 versus Run0 (*bottom*, injection at $z = 1$). The additional grey lines give the $D \propto t^{3/2}$, $\propto t$ and $\propto t^{1/2}$ trends to guide the eye.

magnetic field strength averaged along the line of sight(s) for different epochs in Run2. The sequence shows how the interaction with the environment, as well as the variations of local conditions experienced by the lobes as they expand, cause variations in the velocity and magnetic field experienced by relativistic particles.

Nevertheless, the activity of radio galaxies in both runs adds additional fluctuations to the dynamical evolution of Lagrangian tracers, especially in the first hundreds of Myr following the AGN bursts. In particular, the magnetisation, temperature, and vorticity of particles tracing jets are found to be significantly higher (up to an order of magnitude) up to ~ 200 – 400 Myr after the release of jets. Interestingly, the magnetic field strengths carried by injected tracers show the largest difference compared to Run0. In the case of Run1, the injected particles carry a significantly higher magnetic field strength even ~ 2 Gyr after their release by jets. For comparison, the typical temperature of the same particles are already indistinguishable from the tracers in Run0 ~ 400 Myr after their injection. Also in Run2, particles released by jets have a significantly higher magnetic field than their counterparts in Run0, up to ~ 1 Gyr after their release. These differences are intriguing, in the sense that the non-thermal energy content of particles tracking jets can carry a long dynamical memory of previous AGN seeding events, unlike their corresponding thermal properties, which seem to carry a much shorter (a factor ~ 2 – 4 here) memory of AGN events. This

is consistent with the thermodynamic radial profiles of the ICM previously studied in Sect. 3.2: the violent mixing of gas phases typically found in galaxy clusters at all times quickly entangles the past energy output from AGN with the cluster atmosphere (which is, after all, the most salient feature of AGN feedback). The fact that the magnetic field properties of a fraction of the ICM gas (directly affected by jets) carries a long lasting memory of seeding events offers a powerful probe into the past activity of AGNs, which can be used by radio observations to assess the energy budget of past feedback events in the lifetime of a cluster, and this is to a larger extent compared to what standard X-ray analysis can do (e.g. de Gasperin et al. 2012; Birzan et al. 2012; Croston et al. 2018).

3.4. The evolution of electron and radio spectra

In our runs, relativistic electrons are always first seeded in the ICM by radio jets and later subject to energy losses or re-acceleration processes, depending on the local gas conditions they encounter during their propagation. Most electrons released by radio galaxies suffer from significant adiabatic losses as the radio lobes expand into the ICM, and hence their radio synchrotron power decreases quickly. However, a fraction of the electrons can undergo further (re)acceleration by shocks and turbulence.

Figure 11 shows the electron acceleration and losses in typical conditions of a dynamical ICM. We give the median values of the timescales for energy losses τ_{loss} , acceleration τ_{acc} , and advection τ_{adv} , using $p = 10^3$ electrons as a reference.

The timescales for shock acceleration (τ_{DSA}) are much shorter because shocks only cover a tiny fraction of the cluster volume. Hence, we show the turbulent re-acceleration timescale, τ_{ASA} (Sect. 2.4). Likewise, the timescale for Coulomb losses (τ_{c}) is much longer than the radiative timescale for IC and synchrotron losses (τ_{rad}) for $p = 10^3$, and hence only the second is displayed in the plot.

We should point out some interesting trends: the radiative loss time for electrons steadily increases with time, following the decrease of the $\propto(1+z)^4$ term related to inverse Compton losses (Eq. (6)). The latter dominates the radiative loss terms considering that the typical magnetic field strength probed by most tracers in cells becomes smaller than the cosmic microwave background (CMB) equivalent field strength most of the time. The contributions of adiabatic compression and expansion often switch roles in their impact on the evolution of particles, that is, from enhancing to decreasing the particle energies, on timescales of ≥ 100 – 200 Myr. In both runs, the particles are first subjected to strong adiabatic losses, followed after 5×10^8 yr by adiabatic gains due to strong compression by the external ICM. Later on, particles follow more erratic sequences of expansion and compression as shock waves cross the ICM. Moreover, particles are dispersed in a less dense ICM, particularly in Run1. The acceleration timescale related to the turbulence also significantly varies during the evolution and depending on the local ICM conditions; in general, turbulent re-acceleration is less efficient in balancing cooling losses for $p = 10^3$ electrons in the Run1 case, at least for half of the simulated evolution, because particles diffuse to a larger cluster radius, where the relative impact of solenoidal turbulence is generally smaller (e.g. Vazza et al. 2017b). An exception is a boost of turbulent acceleration in at least one peripheral sector of the group (~ 11 – 13 Gyr) following the last major merger experienced by the cluster (see Fig. 1).

Conversely, electrons ejected by the radio galaxy in Run2 remains more confined in the innermost ICM, where solenoidal

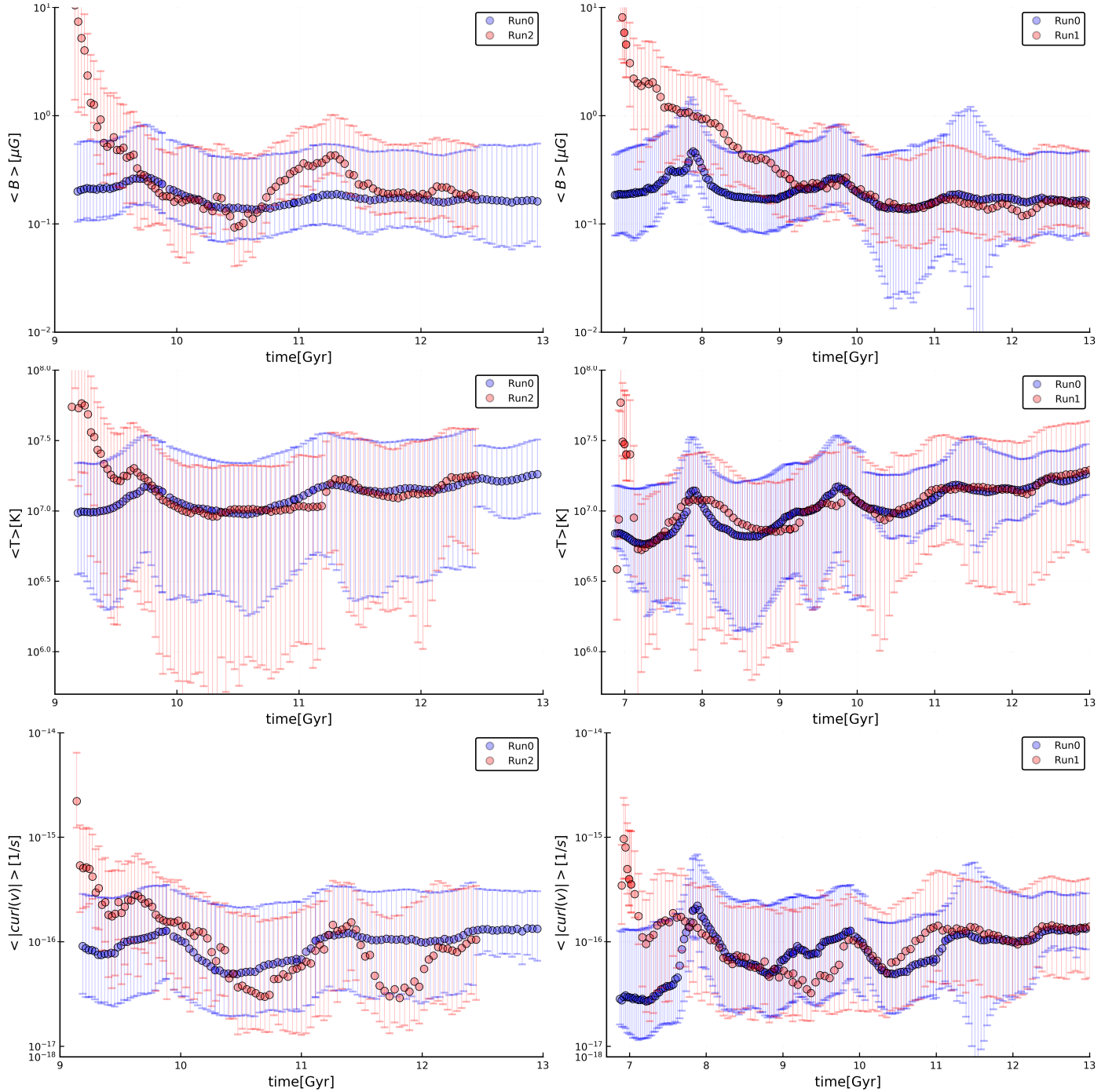


Fig. 8. Evolution of the median magnetic field strength, temperature, and absolute value of vorticity for tracers in our runs (the error bars show the 16–84th percentiles of the distributions at each redshift) comparing Run2 versus Run0 (*left panels*, injection at $z = 0.5$) and Run1 versus Run0 (*right*, injection at $z = 1$). The properties of tracers are measured at each redshift for particles at the radial distance from the cluster centre ≤ 0.5 Mpc.

turbulence is dominant, and the median τ_{ASA} is measured to be smaller than (or of the same order as) the median synchrotron cooling time for $p = 10^3$ electrons for most of the investigated evolution. The complex evolution of the amplitude of different loss and acceleration terms once more stresses the importance of full numerical simulations for a detailed simulation of the full evolution of radio-emitting electrons in a realistic environment.

The panels in Fig. 12 show an example of the spectral energy evolution of 100 electron tracers injected by the radio galaxy in Run2, initially placed in the cells with the highest magnetic field

strength in the jets, roughly corresponding to the location of the brightest emission spots in the southern lobe of Fig. 2. While they are advected at a close distance to each other, these electron tracers are subject to several possible combinations of re-acceleration events (or absence of thereof): only losses, losses and injection and re-acceleration by shocks, losses and only shock re-acceleration, losses and only turbulent re-acceleration, or all mechanisms together, from top to bottom, respectively.

In the presence of cooling and adiabatic losses alone, this family of particles steadily accumulates at a momentum of

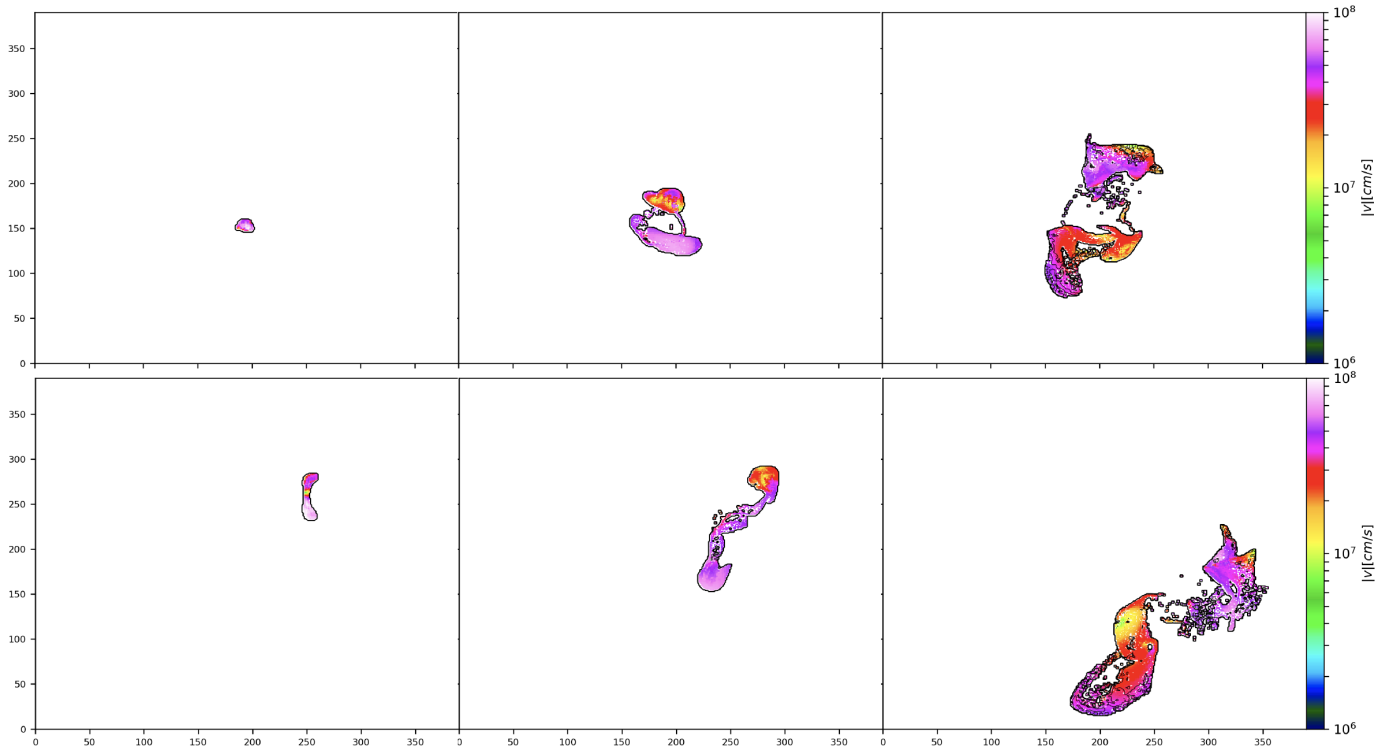


Fig. 9. Velocity magnitude for tracers released by jets in Run2 at three different epochs ($z = 0.46$, $z = 0.37$ and $z = 0.16$ from left to right, respectively), and averaged along the two different lines of sight. *Top row*: evolution of the lobes seen along the line of sight parallel to the jet axis, while *second row*: evolution seen along a perpendicular line of sight (the same as in Fig. 4). The axes are in units of cells of the simulation ($\delta x = 8.86$ kpc co-moving).

$p \sim 10^2$ by the end of the run, consistently with the literature (Brunetti et al. 2001, 2007; Pinzke et al. 2013). The re-acceleration by shocks and turbulence instead largely increases the energy budget of particles in the $p \leq 10^3$ range, while the direct injection of ‘fresh’ electrons by shocks (here seeded by a $\mathcal{M} \sim 3.0$ shock at ~ 2 Gyr after the jet injection), replenishes the high-energy tail of the momentum distribution with a power law. When all the above mechanisms are considered, we can see that the interaction of electrons with the ICM dynamics produces a complex spectrum with several time-dependent features, which overall allows a steep population of radio-emitting electrons to survive several Gyr after the release by radio jets, and overall it generates a more prominent reservoir of low-energy relativistic electrons, for a significant fraction of the lifetime of this galaxy group.

The complete view of the radial distribution in the spectra for different re-acceleration scenarios is given in Figs. 13 and 14. In these figures, we use different line styles to identify the total spectra of all simulated tracers, binned in three different radial shells ($r \leq 300$ kpc with a solid line, $300 \text{ kpc} < r \leq 600$ kpc with a dashed line, and $r > 600$ kpc with a dotted line). We observe a similar evolution at all radii of a complex spectrum (albeit smoothed by the combination of the many more spectra considered here), with tails of $p \geq 10^3$ electrons. This is a consequence of the crossing of shock waves and the steady build-up of a fossil electron reservoir for $p \leq 10^2$ due to the combination of shocks and turbulent re-acceleration. The $p \sim 10^3$ bump caused by turbulent re-acceleration is more evident in Run2, where the electrons remain more confined in the cluster’s innermost regions. In those core regions, $\sim 30\text{--}50\%$ of the volume is typically filled by solenoidal turbulent motions (Vazza et al. 2017b), while only $\leq 0.1\%$ of cells in clusters are

shocked (e.g. Vazza et al. 2009). However, we should point out that our model probably underestimates the highest energy tail of the energy distribution by a factor ~ 2 , owing to the missing term of stochastic turbulent acceleration, the computation of which would require more advanced solvers (e.g. Donnert & Brunetti 2014). Moreover, turbulent re-acceleration is predicted to be more efficient at larger cluster masses (e.g. Cassano & Brunetti 2005; Cassano et al. 2010), hence shorter acceleration times can be expected for more massive objects.

On the other hand, few electrons can exist with momenta larger than a few $\sim 10^2$ if they are only subject to radiative cooling and adiabatic expansion. As seen above, re-accelerated electrons can reach a higher energy in Run2, while in Run1 the bulk of the energy distribution of electrons spreads out to larger cluster radii due to their earlier ejection from their source.

Since enough electrons are only confined in the ICM at late redshift to give rise to potentially detectable radio emission in Run2, we focus on those in the following, and we work out the observable radio properties of this run. The above differences in the energy distribution driven by re-acceleration in the ICM obviously have a direct impact on the observable radio emission that depends on the slope of available CR electrons. The distribution of the radio spectral index of the detectable emission in Run2 at different epochs is shown in Fig. 15. For clarity, only the extreme cases with all re-acceleration terms included, or only with losses, are shown. The radio-weighted distributions are only generated for pixels above the putative detection threshold of a LOFAR LBA observation. As expected, the radio spectral index distribution of models where re-acceleration terms are included shows the marked tendency towards flatter radio spectra. This is compared to the pure cooling scenario at each epoch, and more increasingly in more evolved epochs. For most of their

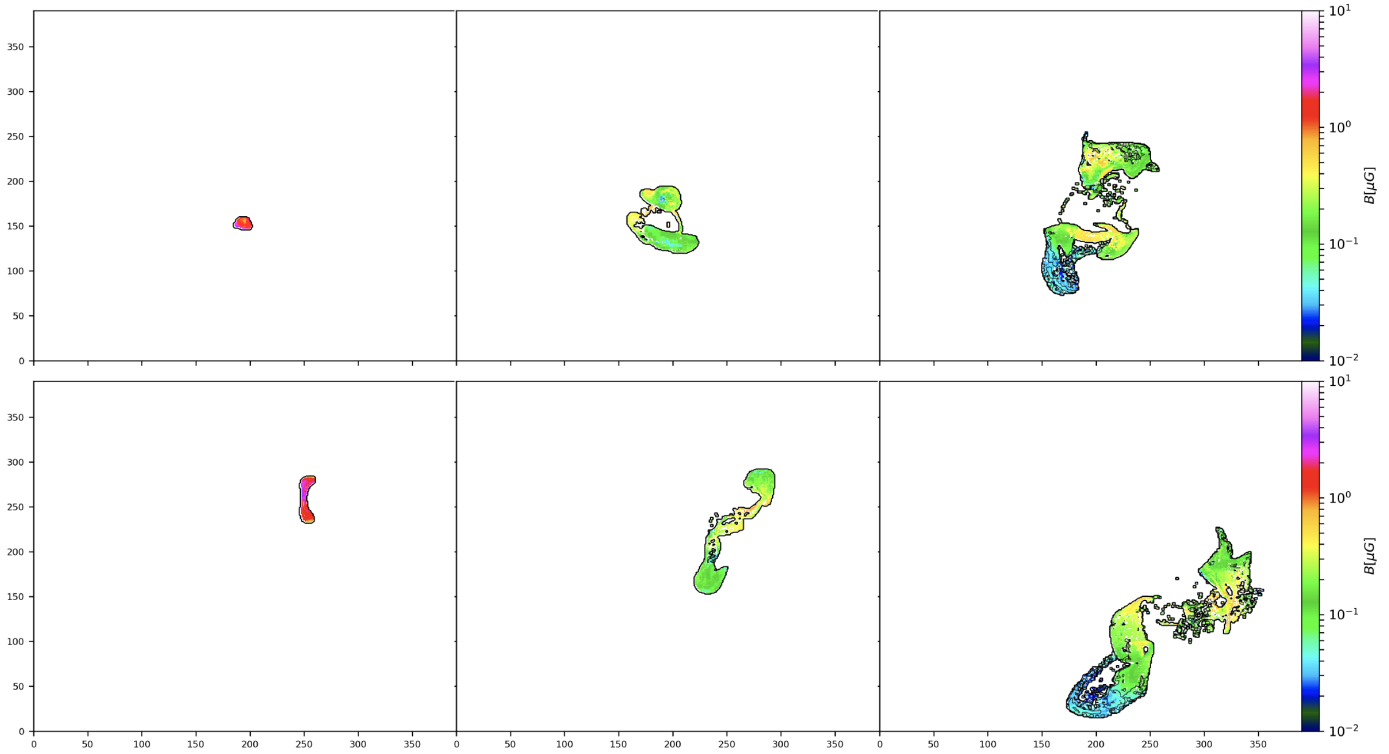


Fig. 10. Magnetic field strength for tracers released by jets in Run2, averaged along the same lines of sight and epochs as in Fig. 9.

evolution after $z \leq 0.4$ in Run2, most of the detectable radio emission from tracers undergoing shock and turbulent re-acceleration has a radio spectrum $\alpha \geq 1.25$ (measured from 50 to 138 MHz), while the residual emission when only cooling and adiabatic losses are included is typically a factor $\Delta\alpha \sim 0.5$ steeper at equal epochs. In general, the steep spectra of fossil electrons in scenarios without re-acceleration from the ICM make them difficult to observe at low frequencies (≤ 140 MHz), and almost invisible at high frequencies (≥ 1.4 GHz).

Figure 16 gives an overview of the radio emission at 140 MHz for electrons in Run2. We compare the three re-acceleration scenarios and only display the emission above the approximate $\geq 3\sigma$ detection level of LOFAR-LBA ~ 8 h observations (with $\sigma \approx 0.2$ mJy beam $^{-1}$ for a $30'' \times 30''$ resolution beam, e.g. Bonafede et al. 2021), placing our source at a reference distance of $z = 0.1$ in all cases. Figure 17 also shows the emission at 1.4 GHz, limited to the last snapshot of the above panel, only for the detectable emission above a realistic approximate sensitivity of an ~ 5 h observation with the JVLA ($\sigma \approx 7$ μ Jy beam $^{-1}$ for a $5'' \times 5''$ resolution beam; e.g. Rajpurohit et al. 2020). Clearly, fossil electrons injected by radio galaxies can shine in the radio band after a few billions years only when all sources of re-acceleration from the ICM are activated. In the absence of turbulent and shock re-acceleration, the brightest emission patches of fossil electrons can hardly be seen as connected on \sim Mpc scales at high frequencies.

Hence, the late radio morphologies (≥ 2 Gyr since first injection) are entirely determined by the passive advection of fossil electrons in the perturbed ICM. Such structures do not have any clear symmetry, appear entirely different when observed from a different viewing angle, and in general do not show simple distributions of radio spectral indices, as shown in Fig. 18.

Interestingly, some of the observed radio morphologies are qualitatively similar to recent deep LOFAR observations of complex radio structures in nearby galaxy clusters (e.g.

de Gasperin et al. 2017; Ignesti et al. 2020; Botteon et al. 2020a; Mandal et al. 2020). In particular, we would like to point to the rich filamentary structures that are found in and around radio galaxies. For example, Ramatsoku et al. (2020) showed collimated synchrotron threads linking the radio lobes of ESO 137–006. These thin structures are most likely magnetically dominated and resemble the morphology seen in Fig. 15.

A careful comparison to observations is beyond the goal of this paper. However, our results regarding morphology suggest that it will be challenging to relate the age of such radio sources to their original radio galaxy. This is because their evolution appears to be mostly related to their interaction with cluster weather. On the other hand, the extensive theoretical study of all possible re-acceleration scenarios that can take place in the realistic ICM (including for a larger variety of objects and merger scenarios) will have the potential to make such remnants of radio galaxy activity a probe of ICM physics (Jones et al. 2017).

4. Caveats

This paper is only a first step towards a more realistic model of the complex interplay between radio galaxies and their environment, and it is admittedly very limited in several important aspects. First, our runs do not include radiative gas cooling, hence there is no self-consistent coupling between the feeding of gas undergoing overcooling and the duty cycle of SMBH jets. This would introduce a number of numerical and physical complications in the modelling of the ICM, which are not entirely solved in cosmological simulations (e.g. Dubois & Teyssier 2008; Collins et al. 2010; Ruszkowski et al. 2011; Tremmel et al. 2017) but are nevertheless crucial for any realistic modelling of ICM atmospheres (e.g. Voit et al. 2020). While this choice was motivated to better focus on the dynamical effect of the feedback from radio galaxies (or absence thereof) on the amplification of magnetic fields in the ICM and on the

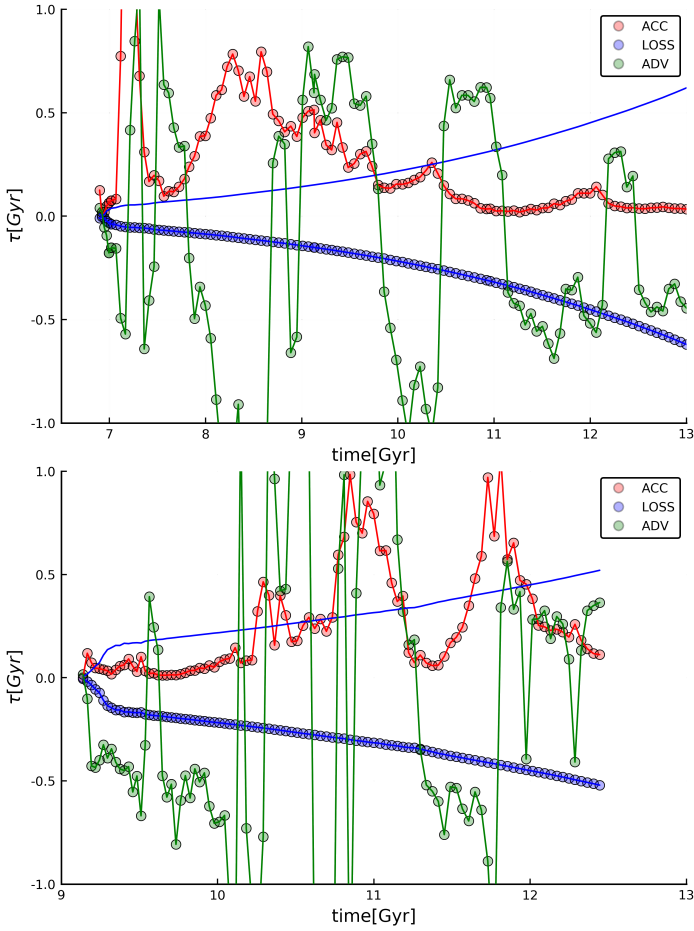


Fig. 11. Evolution of the median timescales for acceleration or losses (see Sect. 2.4) experienced by electrons (here, we consider $\gamma = 10^3$ as a reference) released by radio galaxies in Run1 (*top*) and Run2 (*bottom*). Timescales for loss terms and shown as negative, while timescales for gain terms are shown as positive (to ease the comparison with radiative losses, the latter timescale is also mirrored in the *upper panel*). The timescales for shock acceleration (τ_{DSA}) and for Coulomb losses (τ_{C}) are not visible as they are much smaller and much bigger, respectively, than the time range covered by the vertical axes in the plots.

evolution of relativistic electrons (removed by the additional effects of compression from gas cooling), future developments will have to couple the launching of radio jets with the duty cycle of AGN feedback (e.g. Bourne & Sijacki 2021; Thomas et al. 2021). While our choice to have single and well-defined episodes of jets released by radio galaxies is convenient when studying the dynamics of ejected electrons in a clean way, recent results from radio surveys have instead suggested that at least the most massive radio galaxies can be ‘on’ for most of their lifetime (e.g. Sabater et al. 2019), unlike the discontinuous activity scenario explored in this work. Only through a more consistent coupling of cooling and feedback in our simulations can we approach the complexity of real duty cycles of radio galaxies. The extension of this study with clusters in a different dynamical state will also allow us to explore different combinations of shocks and turbulent re-acceleration events, naturally triggered by different merger configurations.

Secondly, our simulations cannot reproduce the actual interaction between the relativistic (either electron- or proton-dominated) content of jets and the thermal ICM, as our jets are filled entirely with magnetic fields and hot thermal gas, as is

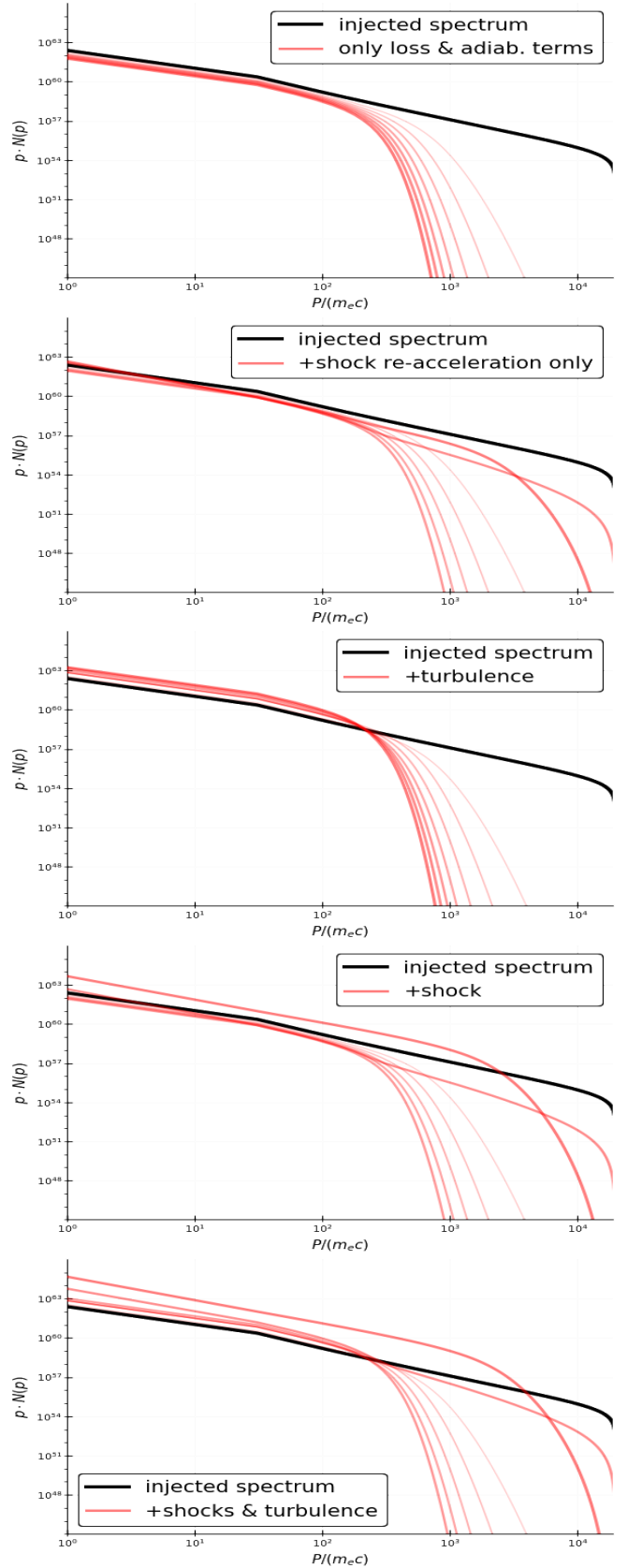


Fig. 12. Evolution (from $z = 0.5$ to $z = 0.1$) of spectral energy distribution of a sample of 100 electron tracers initially located in the most magnetised regions of jets in the Run2 model, for several combinations of re-acceleration scenarios (see labels). The initial particle spectrum is given by the solid black line and the evolution of spectra (equally spaced every ≈ 0.5 Gyr) goes from the most to the least transparent lines.

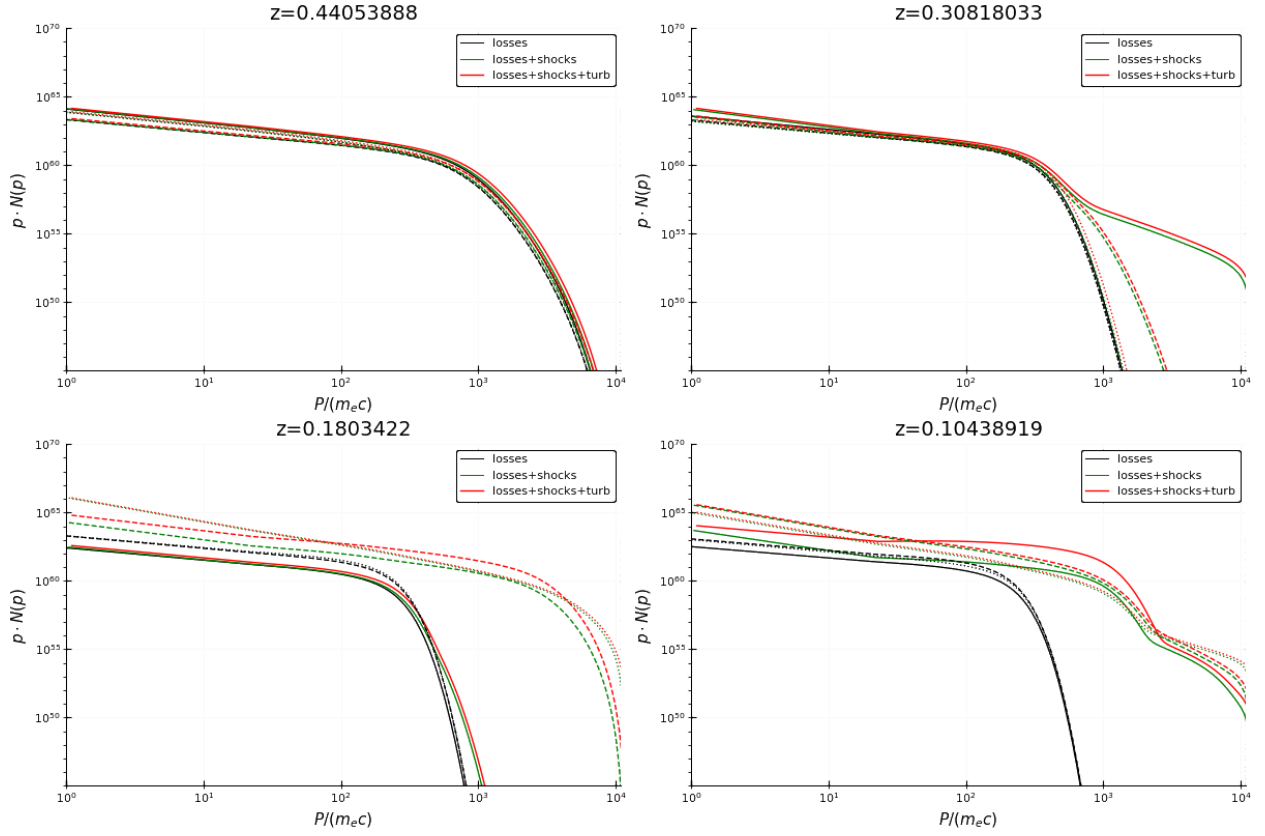


Fig. 13. Evolution of the spectral energy distributions of electrons emitted by the radio galaxy in Run2, for three different acceleration and cooling models (colours) and for three different radial ranges: $r \leq 300$ kpc (solid), $300 \text{ kpc} < r \leq 600$ kpc (dashed), and $r > 600$ kpc (dotted).

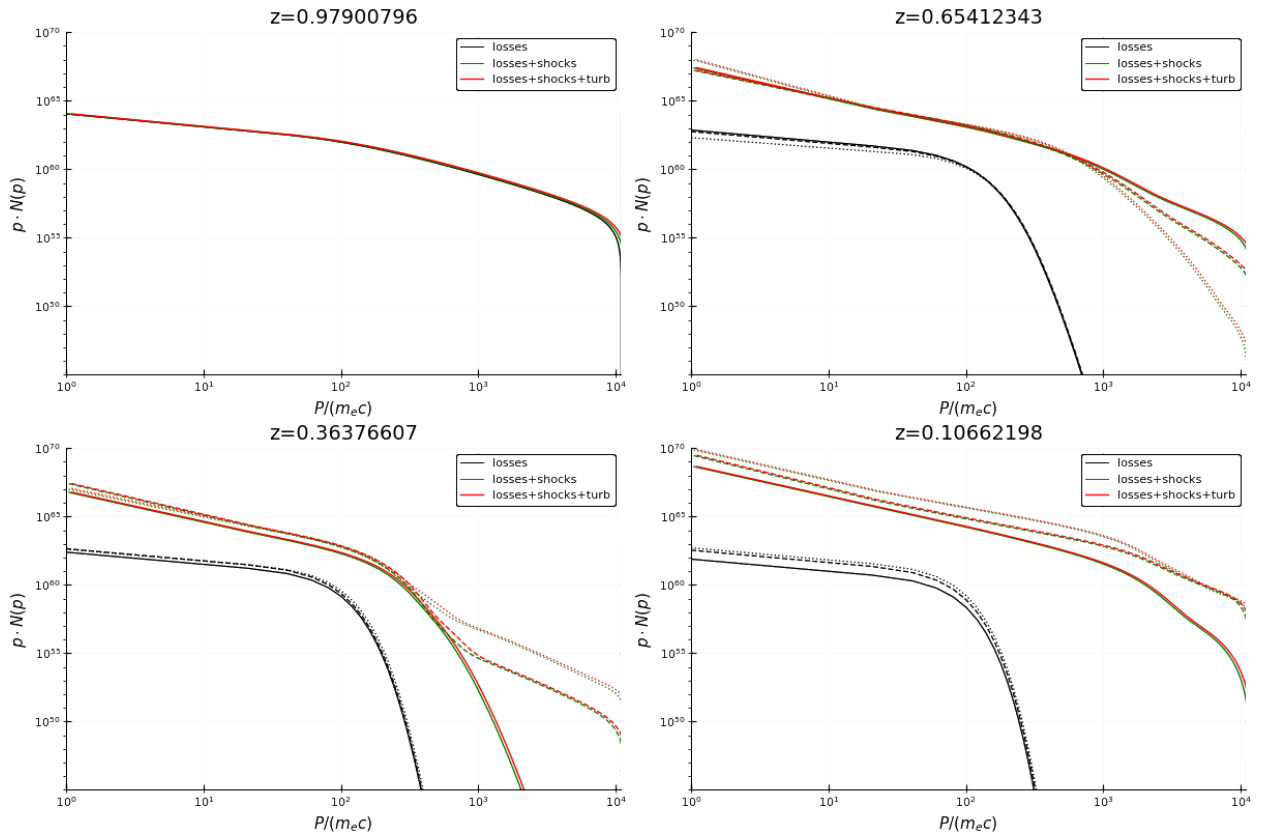


Fig. 14. Evolution of the spectral energy distributions of electrons emitted by the radio galaxy in Run1, for three different acceleration and cooling models (colours) and for three different radial ranges: $r \leq 300$ kpc (solid), $300 \text{ kpc} < r \leq 600$ kpc (dashed), and $r > 600$ kpc (dotted).

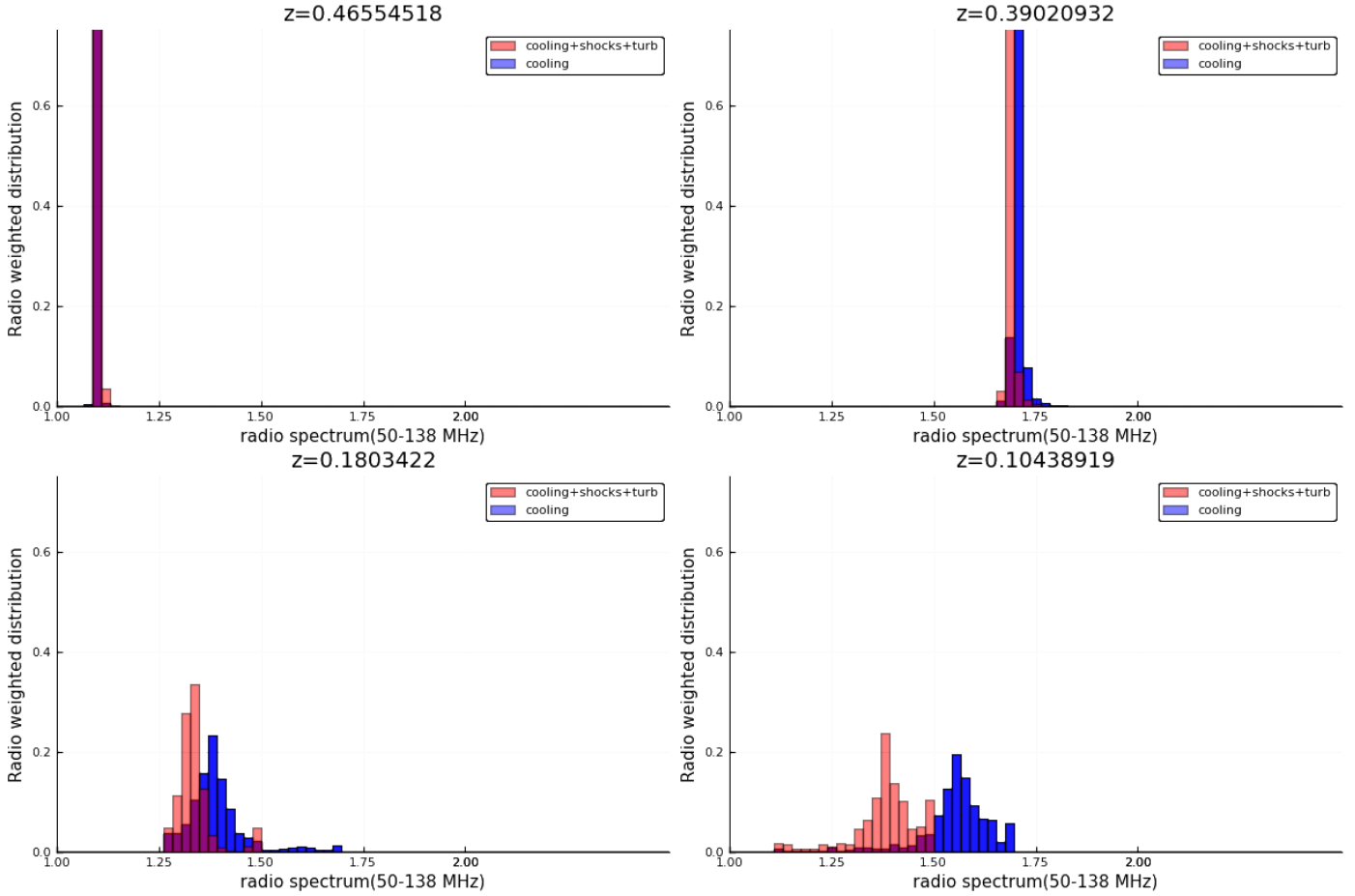


Fig. 15. Evolution of the (radio-power-weighted) distribution of radio spectral index between 50 and 138 MHz, for four epochs in Run2 and only including radio detectable pixels at 50 MHz (assuming a LOFAR LBA observation). Only the cooling and cooling+shocks+turbulence cases are shown for clarity.

commonly the case in simulations of this kind (e.g. Xu et al. 2009; Gaspari et al. 2011; Teyssier et al. 2011). In order to directly test the impact of a significant relativistic energy content in protons or electrons, future development will have to resort to two-fluid modelling of the ICM (e.g. Ehlert et al. 2018; Yang et al. 2019) or similar (e.g. Vazza et al. 2013).

The use of passive tracer particles to track the propagation of relativistic electrons introduces an element of discreteness in our modelling, in the sense that compared to a fluid approach (i.e. via two-fluid modelling; e.g. Girichidis et al. 2020; Ogrodnik et al. 2021), it cannot fully map the spatial diffusion of jet ejecta over time. In this respect, the small-scale morphology of our radio jets may change if the spatial diffusion of relativistic electrons is taken into account, even if the global dynamics of lobes is not expected to change significantly.

Our Fokker-Planck model for particles (Sect. 2.4) is only concerned with specific choices for the acceleration of relativistic electrons via shock waves. It also includes a simplified treatment of the turbulent re-acceleration, in which only a systematic acceleration effect on the global distribution can be captured. Significant effects on the highest energy tail of the electron distributions can be expected for different choices in acceleration scenarios (e.g. Wittor et al. 2020), and will be explored in future work with more sophisticated numerical schemes (e.g. Donnert & Brunetti 2014).

Finally, our simulations only evolved a $P_M = R_M/R_e = \nu/\eta \approx 1$ plasma, meaning a plasma in which the resistivity and

viscosity are of the same order and are numerical by nature. This is clearly a strong and probably unrealistic assumption for the ICM (e.g. Schekochihin et al. 2004; Brunetti & Lazarian 2011; Beresnyak & Miniati 2016), but more expensive, fully kinetic simulations will be required to address the small-scale dynamo in a more realistic way (e.g. Rincon et al. 2016).

5. Conclusions

In this paper, we simulated the evolution of relativistic electrons injected in the ICM by active radio galaxies. Using a Fokker-Planck method on Lagrangian tracer particles, we tracked the cooling and re-acceleration of electrons as a function of time. These new simulations allow us to start a detailed exploration of the idea that diffuse radio emission in the intracluster medium requires a volume-filling population of old relativistic electrons, seeded by radio galaxies (e.g. Jaffe 1977; Schlickeiser et al. 1987; Sarazin 1999; Brunetti et al. 2001). Understanding how radio jets disperse their relativistic and magnetic content on \sim Mpc scales has been shown to be critical to explaining how radio halos, radio relics, mini radio halos, and radio bridges power their large-scale emission; current models need to postulate the existence of a ubiquitous, volume-filling reservoir of ‘fossil’ $\gamma \sim 10^2-10^3$ electrons to account for the normalisation of the observed emission (see Brunetti & Jones 2014; van Weeren et al. 2019). However, the existence of such a

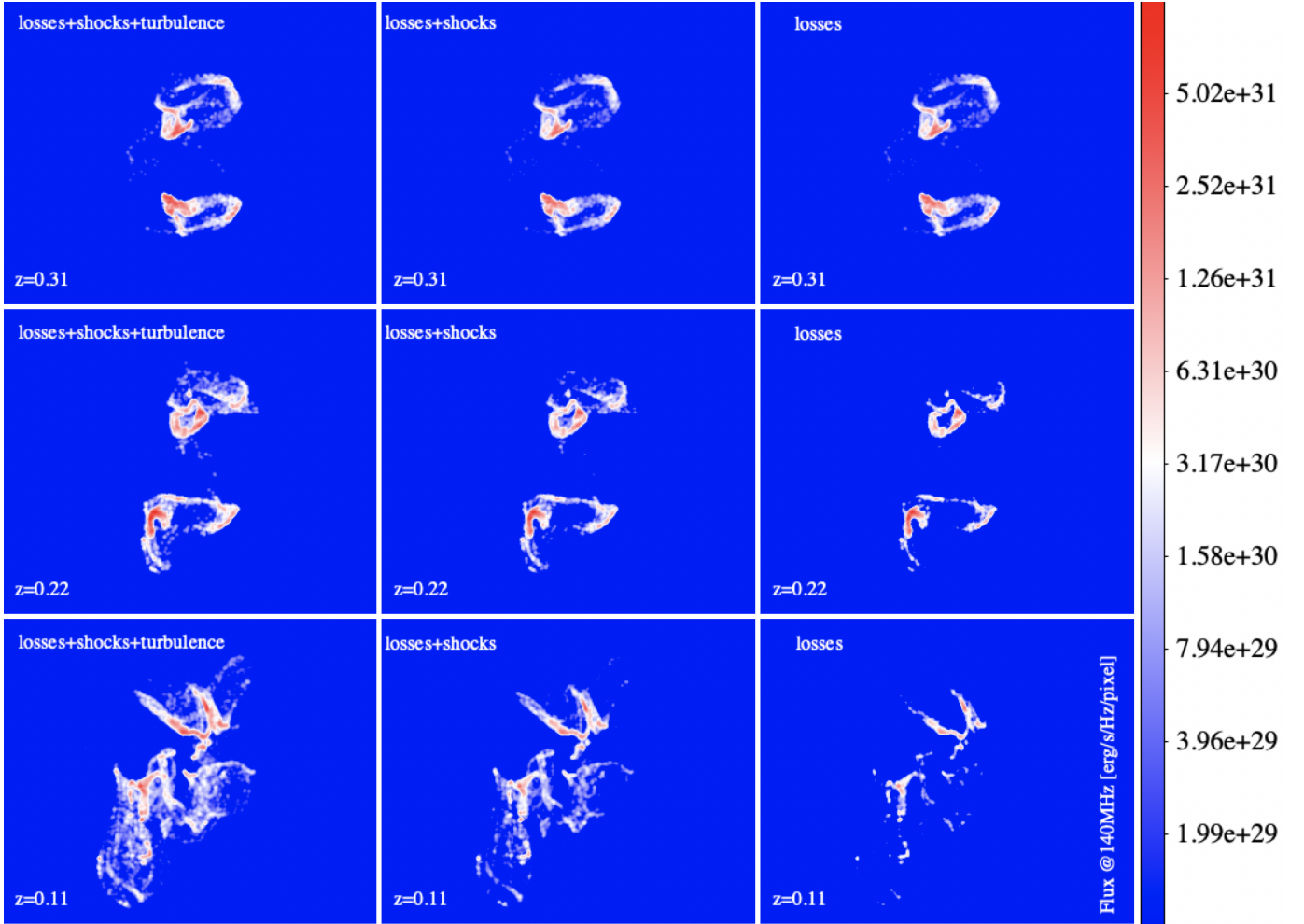


Fig. 16. Evolution of the radio emission for Run2, for three epochs and the three re-acceleration models investigated in the paper. Only the emission above the putative 3σ detectability using LOFAR-HBA (140 MHz) is shown.

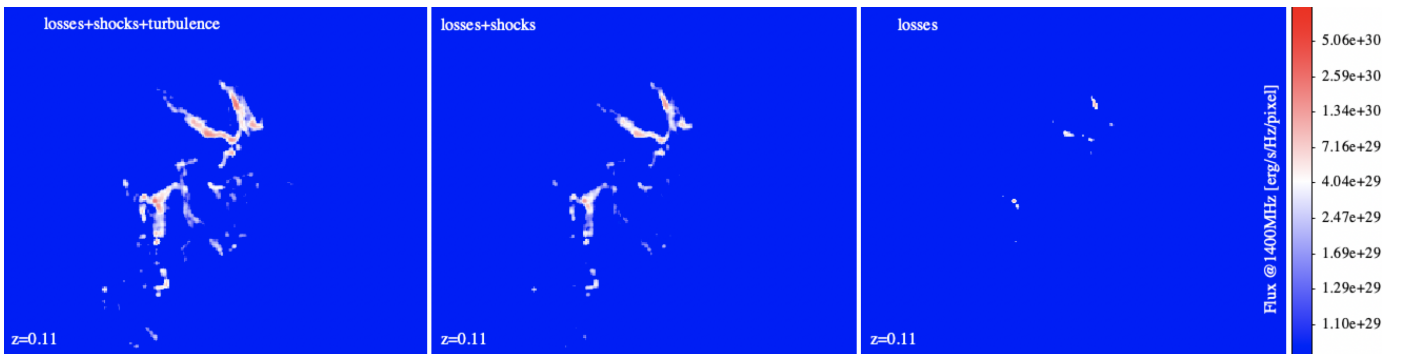


Fig. 17. Radio emission for Run2 at 1.4 GHz, for the three re-acceleration models investigated in the paper. Only the emission above the putative 3σ detectability using JVLA is shown.

reservoir is a mere hypothesis, and whether or not radio galaxies could produce them in their lifetime remains unproven.

Our analysis shows that relativistic electrons from radio galaxies efficiently spread across the intracluster volume as a result of cluster-wide turbulence and the momentum of powerful jets, even considering a single episode of jet injection in the lifetime of a radio galaxy. Close to the injection epoch, we find that the magnetic output of jets dominates close to the radio galaxies (≤ 500 kpc). Yet, the large-scale distribution of magnetic fields seems to be dominated by the growth of the galaxy

cluster. Hence, the input from jets is subdominant with respect to the overall cluster magnetic field, with the exception of the cavities inflated by jets, which preserve a higher and distinct magnetic field up to ~ 2 Gyr after the jet release.

Meanwhile, the cosmic-ray electrons deposited by jets into the ICM steadily build (at least part of) the reservoir of suprathermal particles, which can be further re-accelerated by shock waves and turbulence. However, the final energy (and radio) distributions critically depend on the details of (re)acceleration events caused by shock waves and turbulence. Spatially and

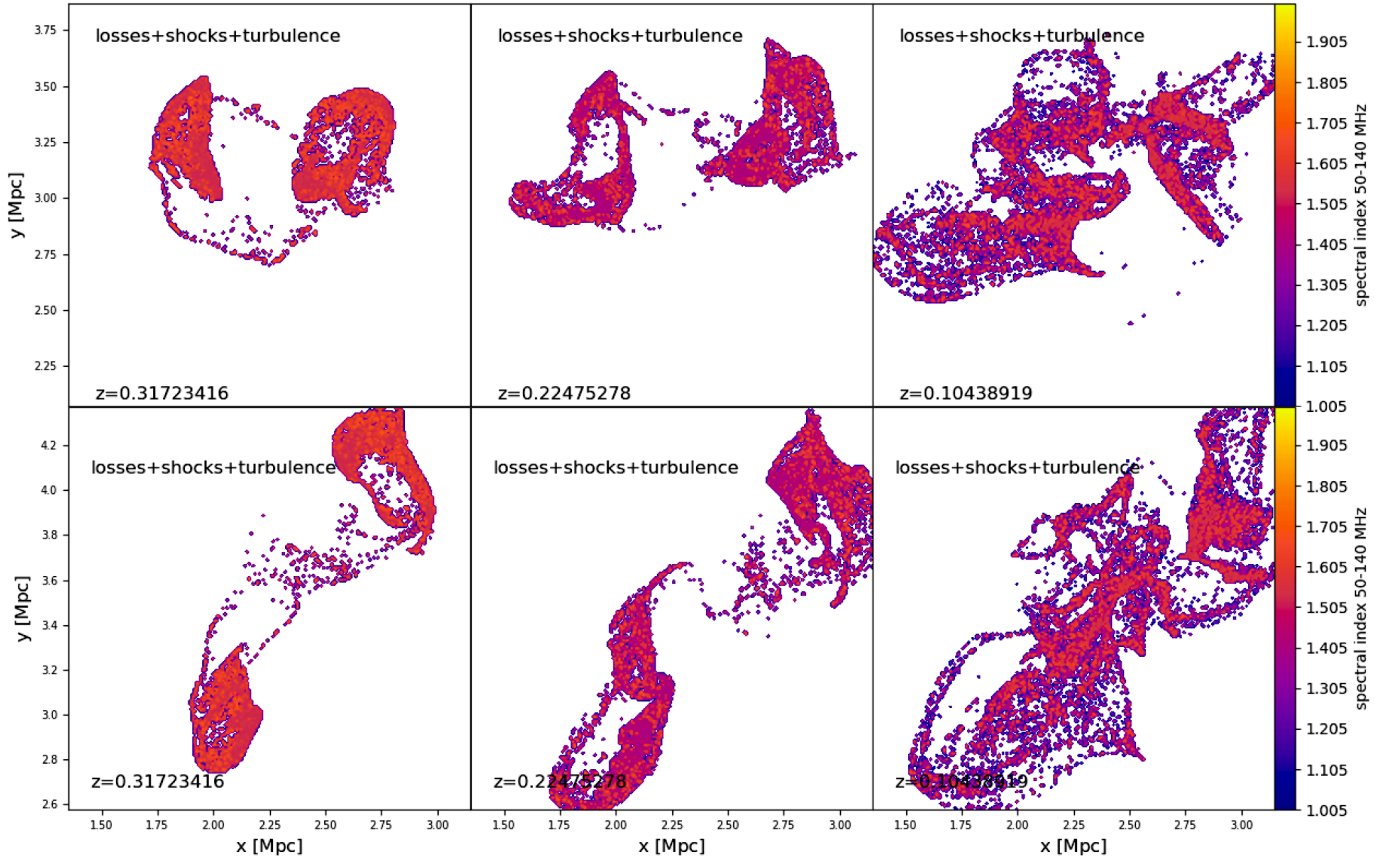


Fig. 18. Radio spectral index maps for the 50–140 MHz range, for three epochs and two lines of sight, for the Run2 simulation. Only regions detectable with LOFAR-HBA (as in Fig. 16) are shown.

spectrally resolved radio observations (especially in the low-frequency regime explored by LOFAR, MWA, and in the future by the SKA-LOW) will be able to retrace the sequence of radio-mode feedback and probe a number of plasma processes (e.g. Hodgson et al. 2021).

In conclusion, electrons and magnetic fields seeded by radio galaxies, or AGN in general, are becoming an additional and required ingredient for cosmological simulations to properly model the complexity of non-thermal emission in groups and clusters of galaxies, and this work represents a first and already very informative step in this direction.

Acknowledgements. We are grateful to the anonymous referee for their helpful comments on the first draft of this work. The authors gratefully acknowledge the Gauss Centre for Supercomputing e.V. (www.gauss-centre.eu) for supporting this project by providing computing time through the John von Neumann Institute for Computing (NIC) on the GCS Supercomputer JUWELS at Jülich Supercomputing Centre (JSC), under projects “stressicm” and projects no. 11823, 10755 and 9016 as well as hhh44. F.V. acknowledges financial support from the European Union’s Horizon 2020 program under the ERC Starting Grant “MAGCOW”, no. 714196. D.W. is funded by the Deutsche Forschungsgemeinschaft (DFG, German Research Foundation) – 441694982. M.B. acknowledges support from the Deutsche Forschungsgemeinschaft under Germany’s Excellence Strategy – EXC 2121 “Quantum Universe” – 390833306. We also acknowledge the usage of online storage tools kindly provided by the Inaf Astronomica Archive (IA2) initiative (<http://www.ia2.inaf.it>) and of the Cosmological Calculator by N. Wright (<http://www.astro.ucla.edu/~wright/CosmoCalc.html>). We gratefully acknowledge helpful scientific discussions with M. Brienza and E. Vardoulaki, concerning details of radio observations of radio galaxies.

References

Abdulla, Z., Carlstrom, J. E., Mantz, A. B., et al. 2019, *ApJ*, 871, 195

- Ackermann, M., Ajello, M., Albert, A., et al. 2014, *ApJ*, 787, 18
 Angelinelli, M., Vazza, F., Giocoli, C., et al. 2020, *MNRAS*, 495, 864
 Banfi, S., Vazza, F., & Wittor, D. 2020, *MNRAS*, 496, 3648
 Beresnyak, A., & Miniati, F. 2016, *ApJ*, 817, 127
 Berezhinsky, V. S., Blasi, P., & Ptuskin, V. S. 1997, *ApJ*, 487, 529
 Bîrzan, L., Rafferty, D. A., Nulsen, P. E. J., et al. 2012, *MNRAS*, 427, 3468
 Bîrzan, L., Rafferty, D. A., Brüggén, M., et al. 2020, *MNRAS*, 496, 2613
 Bodo, G., Rossi, P., Massaglia, S., et al. 1998, *A&A*, 333, 1117
 Bonafede, A., Intema, H. T., Brüggén, M., et al. 2014, *ApJ*, 785, 1
 Bonafede, A., Brunetti, G., Vazza, F., et al. 2021, *ApJ*, 907, 32
 Booth, C. M., & Schaye, J. 2009, *MNRAS*, 398, 53
 Borse, N., Acharya, S., Vaidya, B., et al. 2021, *A&A*, 649, A150
 Botteon, A., Brunetti, G., van Weeren, R. J., et al. 2020a, *ApJ*, 897, 93
 Botteon, A., Brunetti, G., Ryu, D., & Roh, S. 2020b, *A&A*, 634, A64
 Bourne, M. A., & Sijacki, D. 2021, *MNRAS*, 506, 488
 Brighenti, F., & Mathews, W. G. 2000, *ApJ*, 535, 650
 Brüggén, M., & Kaiser, C. R. 2002, *Nature*, 418, 301
 Brüggén, M., Reiprich, T. H., Bulbul, E., et al. 2021, *A&A*, 647, A3
 Brunetti, G., & Jones, T. W. 2014, *Int. J. Mod. Phys. D*, 23, 1430007
 Brunetti, G., & Lazarian, A. 2011, *MNRAS*, 410, 127
 Brunetti, G., & Lazarian, A. 2016, *MNRAS*, 458, 2584
 Brunetti, G., & Vazza, F. 2020, *Phys. Rev. Lett.*, 124, 051101
 Brunetti, G., Setti, G., Feretti, L., & Giovannini, G. 2001, *MNRAS*, 320, 365
 Brunetti, G., Venturi, T., Dallacasa, D., et al. 2007, *ApJ*, 670, L5
 Bryan, G. L., Norman, M. L., O’Shea, B. W., et al. 2014, *ApJS*, 211, 19
 Bykov, A. M., Vazza, F., Kropotina, J. A., Levenfish, K. P., & Paerels, F. B. S. 2019, *Space Sci. Rev.*, 215, 14
 Candelaresi, S., & Del Sordo, F. 2020, *ApJ*, 896, 86
 Capetti, A., Baldi, R. D., Brienza, M., Morganti, R., & Giovannini, G. 2019, *A&A*, 631, A176
 Cassano, R., & Brunetti, G. 2005, *MNRAS*, 357, 1313
 Cassano, R., Etori, S., Giacintucci, S., et al. 2010, *ApJ*, 721, L82
 Chang, J. S., & Cooper, G. 1970, *J. Comput. Phys.*, 6, 1
 Churazov, E., Brüggén, M., Kaiser, C. R., Böhringer, H., & Forman, W. 2001, *ApJ*, 554, 261
 Collins, D. C., Xu, H., Norman, M. L., Li, H., & Li, S. 2010, *ApJS*, 186, 308

- Croston, J. H., Ineson, J., & Hardcastle, M. J. 2018, *MNRAS*, 476, 1614
- de Gasperin, F., Orrú, E., Murgia, M., et al. 2012, *A&A*, 547, A56
- de Gasperin, F., Intema, H. T., Shimwell, T. W., et al. 2017, *Sci. Adv.*, 3, e1701634
- Domínguez-Fernández, P., Vazza, F., Brügger, M., & Brunetti, G. 2019, *MNRAS*, 486, 623
- Donnert, J., & Brunetti, G. 2014, *MNRAS*, 443, 3564
- Donnert, J., Vazza, F., Brügger, M., & Zuhone, J. 2018, *Space Sci. Rev.*, 214, A122
- Dubois, Y., & Teyssier, R. 2008, *A&A*, 482, L13
- Dubois, Y., Devriendt, J., Slyz, A., & Teyssier, R. 2010, *MNRAS*, 409, 985
- Ehlert, K., Weinberger, R., Pfrommer, C., Pakmor, R., & Springel, V. 2018, *MNRAS*, 481, 2878
- Ehlert, K., Weinberger, R., Pfrommer, C., & Springel, V. 2021, *MNRAS*, 503, 1327
- Fabjan, D., Borgani, S., Tornatore, L., et al. 2010, *MNRAS*, 401, 1670
- Fanaroff, B. L., & Riley, J. M. 1974, *MNRAS*, 167, 31
- Furlanetto, S. R., & Loeb, A. 2001, *ApJ*, 556, 619
- Gabici, S., & Blasi, P. 2003, *ApJ*, 583, 695
- Gaspari, M., Brighenti, F., D'Ercole, A., & Melioli, C. 2011, *MNRAS*, 415, 1549
- Gaspari, M., Ruszkowski, M., & Sharma, P. 2012, *ApJ*, 746, 94
- Gendron-Marsolais, M.-L., Hull, C. L. H., Perley, R., et al. 2021, *ApJ*, 911, 56
- Girichidis, P., Pfrommer, C., Hanasz, M., & Naab, T. 2020, *MNRAS*, 491, 993
- Guo, X., Sironi, L., & Narayan, R. 2014a, *ApJ*, 794, 153
- Guo, X., Sironi, L., & Narayan, R. 2014b, *ApJ*, 797, 47
- Hahn, O., & Abel, T. 2011, *MNRAS*, 415, 2101
- Hardcastle, M. J., & Croston, J. H. 2020, *New Astron. Rev.*, 88, 101539
- Hardcastle, M. J., & Krause, M. G. H. 2014, *MNRAS*, 443, 1482
- Heinz, S., Brügger, M., Young, A., & Levesque, E. 2006, *MNRAS*, 373, L65
- Hodgson, T., Bartalucci, I., Johnston-Hollitt, M., et al. 2021, *ApJ*, 909, 198
- Iapichino, L., & Niemeyer, J. C. 2008, *MNRAS*, 388, 1089
- Ignesti, A., Shimwell, T., Brunetti, G., et al. 2020, *A&A*, 643, A172
- Jaffe, W. J. 1977, *ApJ*, 212, 1
- Jaffe, W. J., & Perola, G. C. 1973, *A&A*, 26, 423
- Jones, T. W., Nolting, C., O'Neill, B. J., & Mendygral, P. J. 2017, *Phys. Plasmas*, 24, 041402
- Kaiser, C. R., & Alexander, P. 1997, *MNRAS*, 286, 215
- Kang, H. 2018, *J. Korean Astron. Soc.*, 51, 185
- Kang, H., & Jones, T. W. 2007, *Astropart. Phys.*, 28, 232
- Kang, H., & Ryu, D. 2011, *ApJ*, 734, 18
- Kang, H., Ryu, D., & Jones, T. W. 2012, *ApJ*, 756, 97
- Kardashev, N. S. 1962, *Sov. Astron.*, 6, 317
- Kim, J.-H., Wise, J. H., Alvarez, M. A., & Abel, T. 2011, *ApJ*, 738, 54
- Kronberg, P. P., Lesch, H., & Hopp, U. 1999, *ApJ*, 511, 56
- Lau, E. T., Kravtsov, A. V., & Nagai, D. 2009, *ApJ*, 705, 1129
- Locatelli, N., Vazza, F., & Domínguez-Fernández, P. 2018, *Galaxies*, 6, 128
- Mandal, S., Intema, H. T., van Weeren, R. J., et al. 2020, *A&A*, 634, A4
- Markevitch, M., Govoni, F., Brunetti, G., & Jerius, D. 2005, *ApJ*, 627, 733
- Massaglia, S., Bodo, G., Rossi, P., Capetti, S., & Mignone, A. 2016, *A&A*, 596, A12
- Massaglia, S., Bodo, G., Rossi, P., Capetti, S., & Mignone, A. 2019, *A&A*, 621, A132
- Mathews, W. G., & Brighenti, F. 2007, *ApJ*, 660, 1137
- McCarthy, I. G., Schaye, J., Ponman, T. J., et al. 2010, *MNRAS*, 406, 822
- McCourt, M., Parrish, I. J., Sharma, P., & Quataert, E. 2011, *MNRAS*, 413, 1295
- Mendygral, P. J., Jones, T. W., & Dolag, K. 2012, *ApJ*, 750, 166
- Mignone, A., Massaglia, S., & Bodo, G. 2005, *Space Sci. Rev.*, 121, 21
- Mignone, A., Rossi, P., Bodo, G., Ferrari, A., & Massaglia, S. 2010, *MNRAS*, 402, 7
- Mingo, B., Croston, J. H., Hardcastle, M. J., et al. 2019, *MNRAS*, 488, 2701
- Miniati, F. 2014, *ApJ*, 782, 21
- Nolting, C., Jones, T. W., O'Neill, B. J., & Mendygral, P. J. 2019a, *ApJ*, 876, 154
- Nolting, C., Jones, T. W., O'Neill, B. J., & Mendygral, P. J. 2019b, *ApJ*, 885, 80
- Norman, M. L., & Bryan, G. L. 1999, in *The Radio Galaxy Messier 87*, eds. H. J. Röser, & K. Meisenheimer (Berlin: Springer-Verlag), *Lect. Notes Phys.*, 530, 106
- Norman, M. L., Winkler, K. H. A., Smarr, L., & Smith, M. D. 1982, *A&A*, 113, 285
- Ogrodnik, M., Hanasz, M., & Wólfarński, D. 2021, *ApJS*, 253, 18
- O'Neill, S. M., & Jones, T. W. 2010, *ApJ*, 710, 180
- Owen, F. N., Rudnick, L., Eilek, J., et al. 2014, *ApJ*, 794, 24
- Perucho, M., & Martí, J. M. 2007, *MNRAS*, 382, 526
- Pinzke, A., Oh, S. P., & Pfrommer, C. 2013, *MNRAS*, 435, 1061
- Planck Collaboration XIII. 2016, *A&A*, 594, A13
- Puchwein, E., Sijacki, D., & Springel, V. 2008, *ApJ*, 687, L53
- Rajpurohit, K., Hoeft, M., Vazza, F., et al. 2020, *A&A*, 636, A30
- Ramatsoku, M., Murgia, M., Vacca, V., et al. 2020, *A&A*, 636, L1
- Rasia, E., Borgani, S., Murante, G., et al. 2015, *ApJ*, 813, L17
- Ricarte, A., Tremmel, M., Natarajan, P., & Quinn, T. 2019, *MNRAS*, 489, 802
- Rincon, F., Califano, F., Schekochihin, A. A., & Valentini, F. 2016, *Proc. Natl. Acad. Sci.*, 113, 3950
- Riquelme, M. A., & Spitkovsky, A. 2011, *ApJ*, 733, 63
- Ruszkowski, M., Enblin, T. A., Brügger, M., Heinz, S., & Pfrommer, C. 2007, *MNRAS*, 378, 662
- Ruszkowski, M., Lee, D., Brügger, M., Parrish, I., & Oh, S. P. 2011, *ApJ*, 740, 81
- Ryu, D., Kang, H., Hallman, E., & Jones, T. W. 2003, *ApJ*, 593, 599
- Sabater, J., Best, P. N., Hardcastle, M. J., et al. 2019, *A&A*, 622, A17
- Sarazin, C. L. 1999, *ApJ*, 520, 529
- Schekochihin, A. A., Cowley, S. C., Taylor, S. F., Maron, J. L., & McWilliams, J. C. 2004, *ApJ*, 612, 276
- Schlickeiser, R., Sievers, A., & Thiemann, H. 1987, *A&A*, 182, 21
- Sijacki, D., Springel, V., Di Matteo, T., & Hernquist, L. 2007, *MNRAS*, 380, 877
- Stuardi, C., Bonafede, A., Wittor, D., et al. 2019, *MNRAS*, 489, 3905
- Teyssier, R., Moore, B., Martizzi, D., Dubois, Y., & Mayer, L. 2011, *MNRAS*, 414, 195
- Thomas, N., Dave, R., Jarvis, M. J., & Angles-Alcazar, D. 2021, *MNRAS*, 503, 3492
- Tremblay, G. R., Oonk, J. B. R., Combes, F., et al. 2016, *Nature*, 534, 218
- Tremmel, M., Karcher, M., Governato, F., et al. 2017, *MNRAS*, 470, 1121
- Turner, R. J., & Shabala, S. S. 2015, *ApJ*, 806, 59
- Uchiyama, Y., Aharonian, F. A., Tanaka, T., Takahashi, T., & Maeda, Y. 2007, *Nature*, 449, 576
- Vachaspati, T. 2021, *Rep. Prog. Phys.*, 84, 074901
- van Weeren, R. J., Andrade-Santos, F., Dawson, W. A., et al. 2017, *Nat. Astron.*, 1, 0005
- van Weeren, R. J., de Gasperin, F., Akamatsu, H., et al. 2019, *Space Sci. Rev.*, 215, 16
- Vardoulaki, E., Jiménez Andrade, E. F., Karim, A., et al. 2019, *A&A*, 627, A142
- Vardoulaki, E., Jiménez Andrade, E. F., Delvecchio, I., et al. 2021, *A&A*, 648, A102
- Vazza, F., & Brügger, M. 2014, *MNRAS*, 437, 2291
- Vazza, F., Brunetti, G., & Gheller, C. 2009, *MNRAS*, 395, 1333
- Vazza, F., Gheller, C., & Brunetti, G. 2010, *A&A*, 513, A32
- Vazza, F., Brunetti, G., Gheller, C., Brunino, R., & Brügger, M. 2011, *A&A*, 529, A17
- Vazza, F., Brügger, M., & Gheller, C. 2013, *MNRAS*, 428, 2366
- Vazza, F., Eckert, D., Brügger, M., & Huber, B. 2015, *MNRAS*, 451, 2198
- Vazza, F., Brügger, M., Gheller, C., et al. 2017a, *Classical Quantum Gravity*, 34, 234001
- Vazza, F., Jones, T. W., Brügger, M., et al. 2017b, *MNRAS*, 464, 210
- Vazza, F., Brunetti, G., Brügger, M., & Bonafede, A. 2018, *MNRAS*, 474, 1672
- Voit, G. M., Bryan, G. L., Prasad, D., et al. 2020, *ApJ*, 899, 70
- Völk, H. J., & Atoyan, A. M. 1999, *Astropart. Phys.*, 11, 73
- Wilber, A., Brügger, M., Bonafede, A., et al. 2018, *MNRAS*, 473, 3536
- Wittor, D. 2017, PhD Thesis, Universität Hamburg, Germany
- Wittor, D., & Gaspari, M. 2020, *MNRAS*, 498, 4983
- Wittor, D., Vazza, F., & Brügger, M. 2016, *Galaxies*, 4, 71
- Wittor, D., Vazza, F., & Brügger, M. 2017a, *MNRAS*, 464, 4448
- Wittor, D., Jones, T., Vazza, F., & Brügger, M. 2017b, *MNRAS*, 471, 3212
- Wittor, D., Vazza, F., Ryu, D., & Kang, H. 2020, *MNRAS*, 495, L112
- Xie, C., van Weeren, R. J., Lovisari, L., et al. 2020, *A&A*, 636, A3
- Xu, S., & Zhang, B. 2017, *ApJ*, 846, L28
- Xu, H., Li, H., Collins, D. C., Li, S., & Norman, M. L. 2009, *ApJ*, 698, L14
- Xu, H., Li, H., Collins, D. C., Li, S., & Norman, M. L. 2011, *ApJ*, 739, 77
- Xu, R., Spitkovsky, A., & Caprioli, D. 2020, *ApJ*, 897, L41
- Yang, H.-Y. K., Sutter, P. M., & Ricker, P. M. 2012, *MNRAS*, 427, 1614
- Yang, H. Y. K., Gaspari, M., & Marlow, C. 2019, *ApJ*, 871, 6
- Zuhone, J. A., Markevitch, M., & Johnson, R. E. 2010, *ApJ*, 717, 908

Appendix A: Visual impression of the two runs

Figures A.1 and A.2 give the visual impression of the refined evolutions of Run1 and Run2, using the RGB colour-coding of different information: radio emission (shades of pink), X-ray

emission (green), and gas temperature (blue), in all cases applying logarithmic stretching and adjusting the range of values of the colour bar to the changing maximum and minimum values of the fields on display, in order to enhance the visibility of structures⁶.

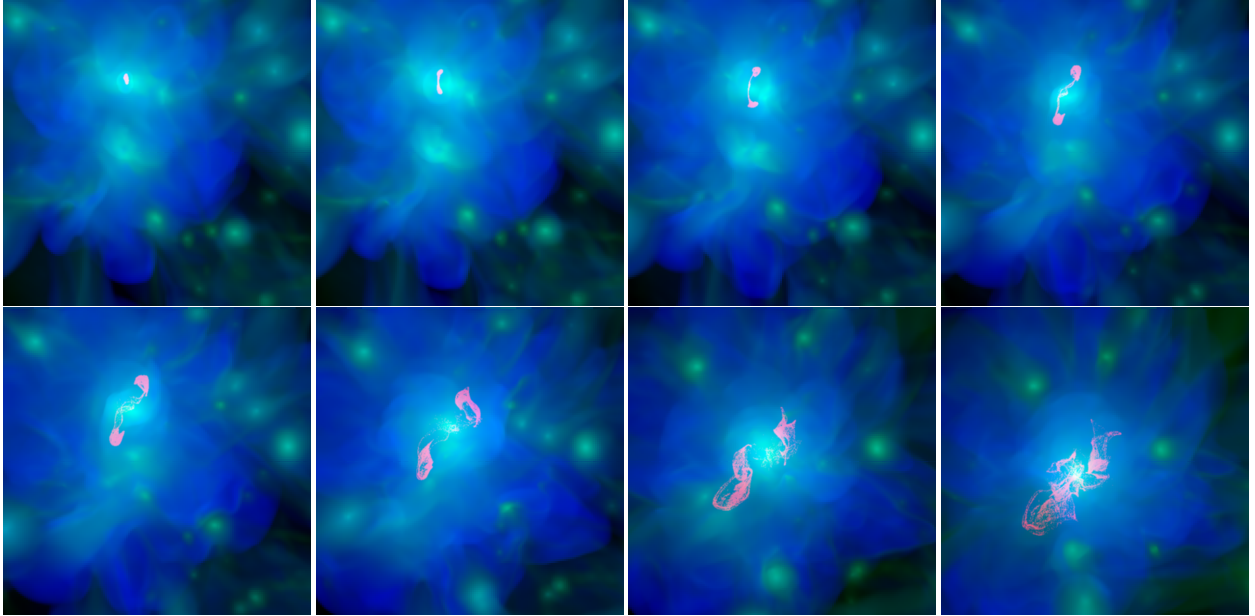


Fig. A.1. Rendering of the evolution of radio emission (shades of pink), X-ray emission (green), and gas temperature (blue) for roughly equally spaced time steps from $z = 0.49$ to $z = 0.1$ in our Run2 simulation. Each image has a side of 5.5 Mpc (co-moving). The movie is available [online](#).

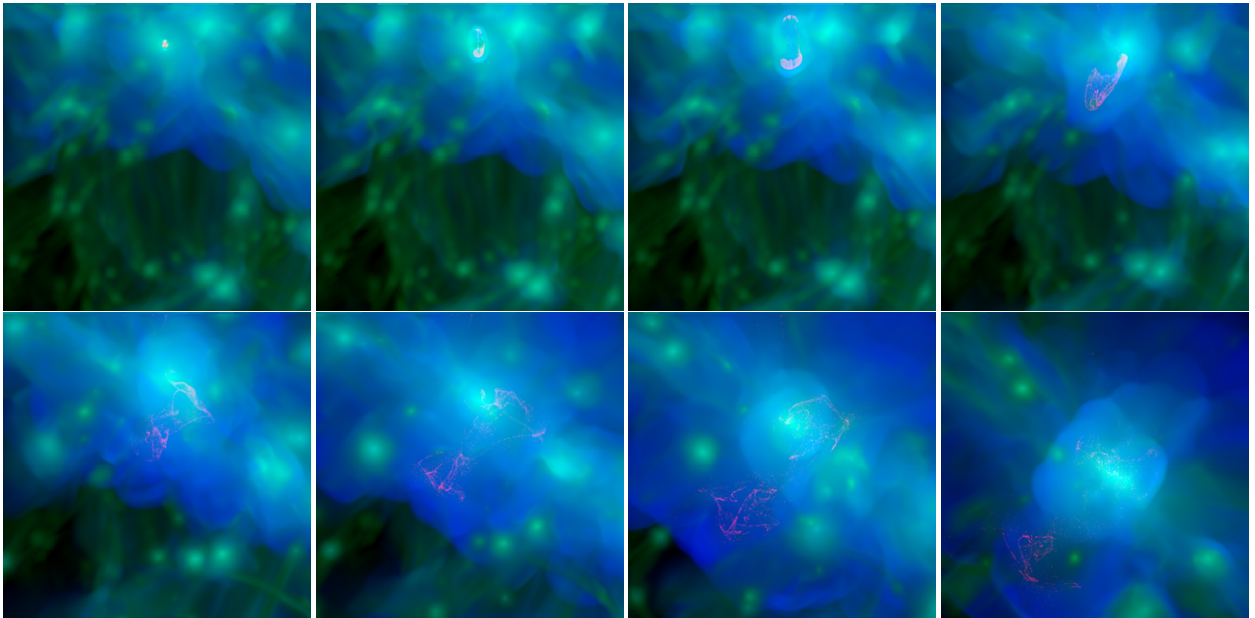


Fig. A.2. Rendering of the evolution of radio emission (shades of pink), X-ray emission (green), and gas temperature (blue) for roughly equally spaced time steps from $z = 0.99$ to $z = 0.1$ in our Run1 simulation. Each image has a side of 5.5 Mpc (co-moving). The movie is available [online](#).

⁶ The full movies of the two simulations can be found online and at <https://vimeo.com/490397871> and <https://vimeo.com/490399056>.